







Basaltic Plinian eruptions at Las Sierras-Masaya volcano driven by cool storage of crystal-rich magmas

Emily C. Bamber ¹✉, Giuseppe La Spina ^{1,2}, Fabio Arzilli^{1,3}, Mattia de' Michieli Vitturi ^{4,5},
Margherita Polacci¹, Margaret E. Hartley ¹, Maurizio Petrelli ⁶, Jonathan Fellowes¹ & Mike Burton ¹

Although rare, basaltic Plinian eruptions represent a considerable volcanic hazard. The low viscosity of crystal-poor basaltic magma inhibits magma fragmentation; however, Las Sierras-Masaya volcano, Nicaragua, has produced multiple basaltic Plinian eruptions. Here, we quantify the geochemistry and volatile concentrations of melt inclusions in samples of the Fontana Lapilli and Masaya Triple Layer eruptions to constrain pre-eruptive conditions. Combining thermometry and geochemical modelling, we show that magma cooled to ~1000 °C prior to eruption, crystallising a mush that was erupted and preserved in scoriae. We use these data in a numerical conduit model, which finds that conditions most conducive to Plinian eruptions are a pre-eruptive temperature <1100 °C and a total crystal content >30 vol.%. Cooling, crystal-rich, large-volume basaltic magma bodies may be hazardous due to their potential to erupt with Plinian magnitude. Rapid ascent rates mean there may only be some minutes between eruption triggering and Plinian activity at Masaya.

¹Department of Earth and Environmental Sciences, The University of Manchester, Oxford Road, Manchester M13 9PL, UK. ²Istituto Nazionale di Geofisica e Vulcanologia - Osservatorio Etneo, Sezione di Catania, Piazza Roma, 2, 95125 Catania, Italy. ³School of Science and Technology, Geology Division, University of Camerino, Camerino, Italy. ⁴Department of Geology, University at Buffalo, Buffalo, NY 14260, USA. ⁵Istituto Nazionale di Geofisica e Vulcanologia, Sezione di Pisa, Via Cesare Battisti, 53, 56125 Pisa, Italy. ⁶Department of Physics and Geology, Università degli Studi di Perugia, Piazza dell'Università, 06123 Perugia, Italy. ✉email: emilycharlotteb@gmail.com

Plinian eruptions represent the extreme endmember of explosive basaltic volcanism. The low viscosity of crystal-poor basaltic magma typically precludes magma fragmentation, but basaltic Plinian eruptions have occurred, such as the 60 ka Fontana Lapilli (FL) and 2.1 ka Masaya Triple Layer (MTL) eruptions of Las Sierras-Masaya volcano, Nicaragua; the 122 BCE Etna eruption, Italy; the 1886 CE Tarawera eruption, New Zealand, and the 2017–2018 CE eruption of Ambae, Vanuatu^{1–7}. Basaltic Plinian eruptions may eject $>1 \text{ km}^3$ of tephra and have high mass eruption rates reaching up to 10^8 kg s^{-1} , sustaining an eruption column over 25 km in height^{2,4,5}, with substantial impacts for communities and the environment. Examples of sub-Plinian basaltic eruptions include the 1085 CE eruption of Sunset Crater, USA⁶. The rapid ascent rates of basaltic magma, estimated between 4–75 m s^{-1} for the 2017–2018 CE Ambae eruption⁷, may lead to large volumes of tephra being ejected within a few minutes of eruption onset, leaving minimal time to implement mitigation procedures. Several mechanisms have been proposed to explain basaltic Plinian eruptions, including syn-eruptive crystallisation, bubble nucleation during rapid ascent, and high initial volatile concentrations^{8–17}.

Las Sierras-Masaya volcanic system is located approximately 25 km south from Nicaragua's capital city, Managua¹⁸ (Fig. 1). The present-day Masaya volcano is very active, producing low-intensity, localised explosive activity and is a large source of magmatic degassing¹⁹ in the Central American Volcanic Arc. However, Masaya caldera has produced several basaltic Plinian eruptions: the 6 ka San Antonio Tephra (SAT), the 2.1 ka MTL and 1.8 ka Masaya Tuff-Ticuan-tepe Lapilli eruptions (MT-TIL)^{13,20}. The 60 ka FL eruption has been associated with the formation of the older Las Sierras caldera, after which the Masaya shield volcano was constructed^{18,20}. Deposits from all these eruptions are found at the present-day location of Managua^{2,3,13,21}.

The last major eruption of juvenile material at Masaya was the 1772 CE lava flow²⁰. Since 1772, approximately 47 km^3 of non-erupted magma is estimated to have been degassed²⁰. Despite the diverse eruptive activity at Las Sierras-Masaya volcanic system, whole-rock compositions of erupted products appear to show chemical homogeneity over 60,000 years, suggesting highly explosive activity is not controlled by variations in magma composition^{20,22,23}. This absence of geochemical cyclicality makes the timescale of a future Plinian eruption difficult to forecast as the transition to an explosive system may not be preceded by an identifiable geochemical change, increasing the volcanic risk posed to the ~ 2 million people who live within the area²⁴.

The aim of this study is to understand the magmatic conditions that could drive a highly explosive eruption of this hazardous volcano. We present a combined petrological and numerical investigation (detailed in Methods) into the conditions which promote Plinian activity at this system, providing new major, trace and volatile element data for the FL and MTL eruptions. We demonstrate that the FL magma experienced a complex pre-eruptive history, stagnating at shallow depth, enabling cooling and crystallisation of a mush within the magma reservoir. We incorporate petrological data on the MTL eruption from this study and Bamber et al.¹⁶ into a numerical conduit model^{25–27} to provide simulations of the conduit dynamics of a basaltic Plinian eruption of Masaya. We correlate the results of our sensitivity analysis to the diverse eruptive history of the volcano.

Results and discussion

The Fontana Lapilli eruption: textural observations and geochemical modelling. FL samples are basaltic andesitic ($\sim 53 \text{ wt.}\%$ SiO_2 ; $\sim 4 \text{ wt.}\%$ total alkalis), with plagioclase (7 vol.%), olivine (1 vol.%) clinopyroxene ($<1 \text{ vol.}\%$) phenocrysts and trace amounts

of magnetite. Microlites ($<100 \mu\text{m}$) often have hopper to swallowtail habits. Microlite phases are plagioclase, clinopyroxene, olivine and magnetite. Scoriae are texturally heterogeneous, with microlite-poor and microlite-rich regions (Fig. 2a), where crystallinity increases from 5 to 63 vol.% and glass varies between 95 and 37 vol.%. Vesicularity varies between 14 and 26 vol.% for the two endmembers. This microtextural heterogeneity is comparable to MTL samples (Fig. 2b–d).

FL samples contain enclaves with a mineralogical assemblage similar to the surrounding matrix (Fig. 2e–h). We define the matrix as the assemblage of phenocrysts, microlites and glass described above. Enclaves have a higher plagioclase and clinopyroxene crystal fraction than the matrix (Supplementary Table 1) and a different habit than microlite matrix crystals despite their comparable size. Enclave crystals may have a crystallisation history distinct from matrix phenocrysts and microlites. Vesicles within enclaves are smaller and more spherical than matrix vesicles. We define two categories of enclaves based on microtextural characteristics, referred to as Type A and Type B. Type A enclaves have features indicative of plastic deformation²⁸, such as irregular contacts with the matrix, subparallel alignment of the mineral assemblage with matrix microlites, and a large interstitial glass component (41–51 vol.%) (Fig. 2e–g). Spherical to sub-spherical vesicles in interstitial glass suggest that Type A enclaves contained dissolved volatiles, vesiculating during magma ascent²⁹. Type B enclaves (Fig. 2h) have regular shaped contacts with the matrix, crystal alignment discordant to that of matrix microlites, and less interstitial glass (11–16 vol.%) with very few vesicles. The area fraction of enclaves ranges between 0.04 and 0.26 and the area of enclaves ranges between $0.3\text{--}0.6 \text{ mm}^2$.

Plagioclase and clinopyroxene (phenocrysts and microlites) compositions within the matrix (An_{51-90} ; $\text{Wo}_{28-46}\text{En}_{35-51}\text{Fs}_{8-23}$) and enclaves (An_{22-69} ; $\text{Wo}_{30-44}\text{En}_{34-51}\text{Fs}_{12-23}$) in FL samples overlap (Supplementary Fig. 1). Enclave hosted olivine crystals are more fayalitic (Fo_{45-68}) than matrix microlites (Fo_{68-73}). Enclave and matrix crystal compositional homogeneity suggests a possible common origin, as phases accumulating within a crystal-rich mush zone of the magma reservoir³⁰. Enclave phases tend to show more evolved compositions, suggesting that they may have crystallised at lower temperatures within the reservoir. Preferred orientation of crystals resembles the sedimentation structures of cumulates (Fig. 2g), trapping interstitial liquid. Preferred orientation of crystals may also indicate flow alignment, but lamination and randomly orientated, sub-spherical vesicles in interstitial glass may be more suggestive of crystal settling, as vesicles are not elongated in the direction of preferred orientation³¹. We interpret Type A enclaves as representative of the mush zone within the storage reservoir³². Type B enclaves have less interstitial glass and occasional small, sub-spherical vesicles and are more likely sourced from the adjacent rigid crust of the mush³². The distribution of Type B enclaves throughout the FL eruption phases suggests continued disaggregation of the mush, as opposed to entrained plutonic fragments which may be concentrated in the opening phase. The mush and its interstitial liquid were preserved within scoriae on eruption and quenching²⁹.

Most FL melt inclusions (MI) are more evolved than the whole-rock composition, showing a decrease in MgO and an enrichment in SiO_2 and alkalis (Fig. 3a–c). MI have been corrected for post-entrapment crystallisation (PEC). Following PEC corrections, most MI are still not in equilibrium with both their host crystals and more anorthite-rich plagioclase crystals (An_{73-90}) (Supplementary Data 1).

FL microlite-poor glass and MI compositions generally overlap. However, some microlite-poor glasses are trachy-andesitic, overlapping with microlite-rich glass. Type A enclave interstitial glasses

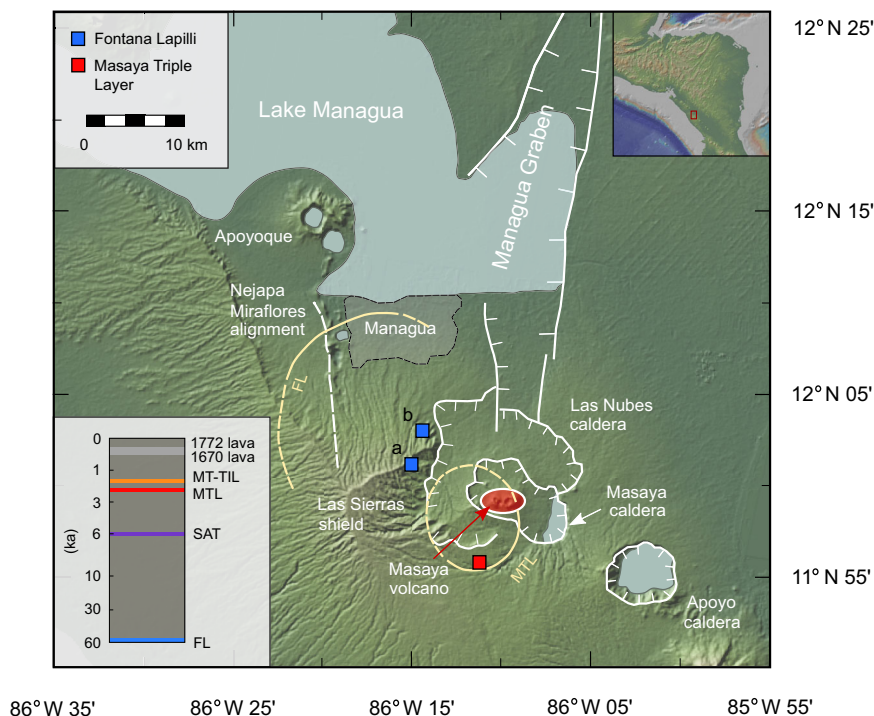


Fig. 1 Map showing the location of Masaya caldera and proximal volcanic and tectonic features. The current active centre of Masaya volcano is highlighted in red. Sampling locations for the FL and MTL eruptions are indicated by blue and red squares respectively. The inset map shows the location of the study area. The stratigraphic column shows the Plinian eruptions of Las Sierras-Masaya volcanic system and the 1670 and 1772 eruptions which produced lava flows²². The 50 cm isopach for the Fontana Lapilli eruption² and the 40 cm isopach for the MTL eruption (subunit II of Pérez et al.³) are highlighted in yellow. Structural features in the Masaya area¹⁸ are highlighted in white. The maps were made using GeoMapApp⁸⁵ (<http://www.geomapapp.org>).

are generally more evolved than FL matrix glass but overlap with trachy-andesitic, microlite-poor glass. Type B enclave interstitial glasses have the most evolved and varied compositions.

We used Rhyolite-MELTS v.1.2³³ to examine the expected liquid compositions that would be generated from the average FL MI composition with progressive cooling and crystallisation. FL compositions measured using EPMA plot upon a common modelled liquid line of descent (LLD) (Fig. 3b, c), indicating melt evolution controlled by plagioclase, clinopyroxene and olivine crystallisation, reaching a total crystallinity of 60 vol.% at 960 °C and 40 MPa (Supplementary Data 2). The modelled crystal fraction at 40 MPa and 980–990 °C agrees with measured Type A enclave crystal fractions (Supplementary Table 1).

Figure 4 shows the distribution of trace elements in glasses and MI (Supplementary Data 3). For FL samples, Sr decreases with increasing Zr, as Sr is compatible in plagioclase, the dominant crystallising phase. Incompatible elements Ba and La increase with increasing Zr. A fractional crystallisation trend was modelled using Petrograph software³⁴ (Fig. 4). FL MI and glasses fit well with the modelled fractional crystallisation trend, indicating crystallisation-controlled melt evolution. According to the fractional crystallisation model, the observed trace element distribution is produced by 50–60 vol.% crystallisation, in agreement with Type A enclaves that have crystal contents of 50–60 vol.%. The microlite-poor, trachy-andesitic melt enriched in incompatible elements but depleted in Sr could originate from expulsion of interstitial melt from the crystal mush on its compaction³⁵, or upon volatile saturation³¹. Melt differentiation models for both FL major and trace element chemistry confirm crystallisation-controlled melt evolution and that it is unlikely that the observed trends were produced by magma mixing³⁶.

PEC-corrected FL MI contain 0.91–2.27 wt. % H₂O and 98–1103 ppm CO₂ (Fig. 5). For FL MI, H₂O and CO₂ concentrations generally decrease with decreasing MgO content. In general, more primitive MI are found in more anorthitic phenocrysts. Calculated FL MI entrapment pressures range between 26 and 189 MPa, assuming volatile saturation at the time of entrapment. However, the CO₂ budget of MI-hosted bubbles has not been measured. Formation of bubbles during MI cooling and PEC can partition CO₂ into the bubble from the glass phase³⁷. MI-hosted bubbles may host up to 40–99% of the total inclusion CO₂^{37–40}; therefore, the MI glass phase provides only a minimum estimate of the pre-eruptive CO₂ content. In turn, our entrapment pressures represent minimum estimates of the storage region depth.

This entrapment pressure range is consistent with Rhyolite-MELTS simulations, which find that the FL mineralogical assemblage cannot be produced at pressures exceeding 200 MPa. At higher pressures, clinopyroxene is the dominant crystallising phase (Supplementary Data 2), but clinopyroxene phenocrysts are rarely observed in our samples. The LLD modelled at a fixed pressure of 200 MPa does not fit our measured glass compositions (Fig. 3).

Modelling a degassing trend using MagmaSat^{41,42} finds that FL MI plot upon a closed-system trend with an initial exsolved vapour content of 5 wt.% (Fig. 5). However, analysis of bubble-bearing MI demonstrates that a degassing trend may be produced by measuring only the MI glass phase and not accounting for the bubble CO₂ content³⁷. For our FL samples, only one MI has a bubble; therefore, our modelled trend most probably represents a true degassing trend rather than being produced by CO₂ loss to MI-hosted bubbles.

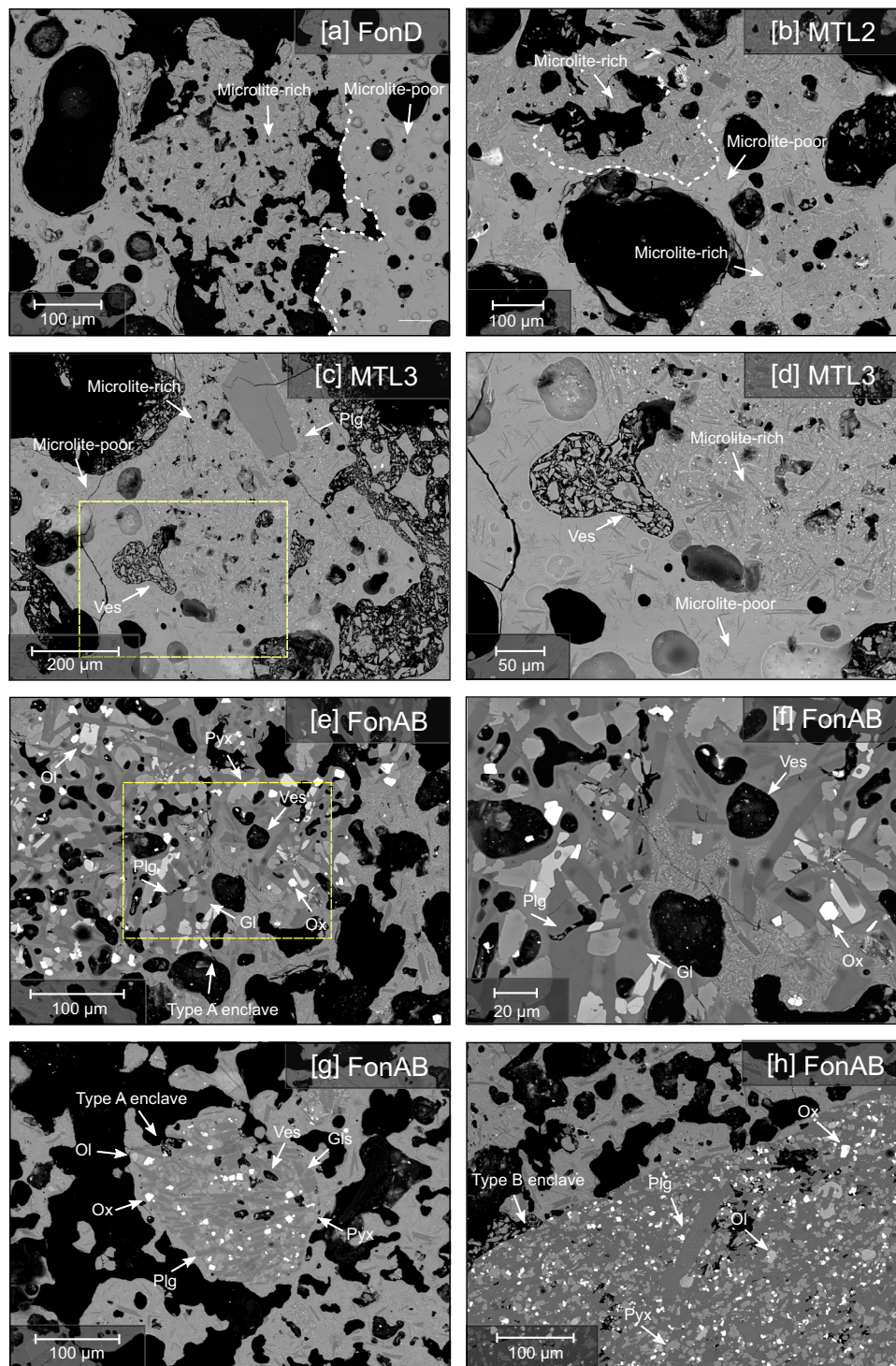


Fig. 2 Back-scattered electron images of key microtextural features observed in scoriae. Scoriae are from the Fontana Lapilli (Fon) (a, e–h) and Masaya Triple Layer (MTL) (b–d) eruptions. (a) Microlite-poor and microlite-rich regions, exhibiting different crystal fractions and vesicle morphologies. The boundary between the two regions is highlighted by the white line. (b) Mingling region between microlite-poor and microlite-rich regions. The white line highlights the boundary between the two regions. (c) Mingling region between microlite-poor and microlite-rich regions. Vesicle size and morphology differs between regions of varying crystallinity. (d) Higher magnification image of (c) showing the larger vesicles which extend into both the microlite-poor and microlite-rich regions. (e) Type A enclave, with an irregular, deformed contact and largely vesiculated (Ves) interstitial glass (G). Plagioclase (Plg), pyroxene (Pgx), olivine (Ol) and oxide (Ox) crystals are labelled. There is subparallel alignment of microlites with the surrounding matrix. (f) Higher magnification image of (e), showing the boundary between the Type A enclave and the matrix and vesicles within the interstitial glass. (g) Type A enclave showing preferred orientation of plagioclase, pyroxene and oxide microlites. (h) Type B enclave, with crystal alignment discordant to surrounding matrix microlites and a small amount of interstitial glass.

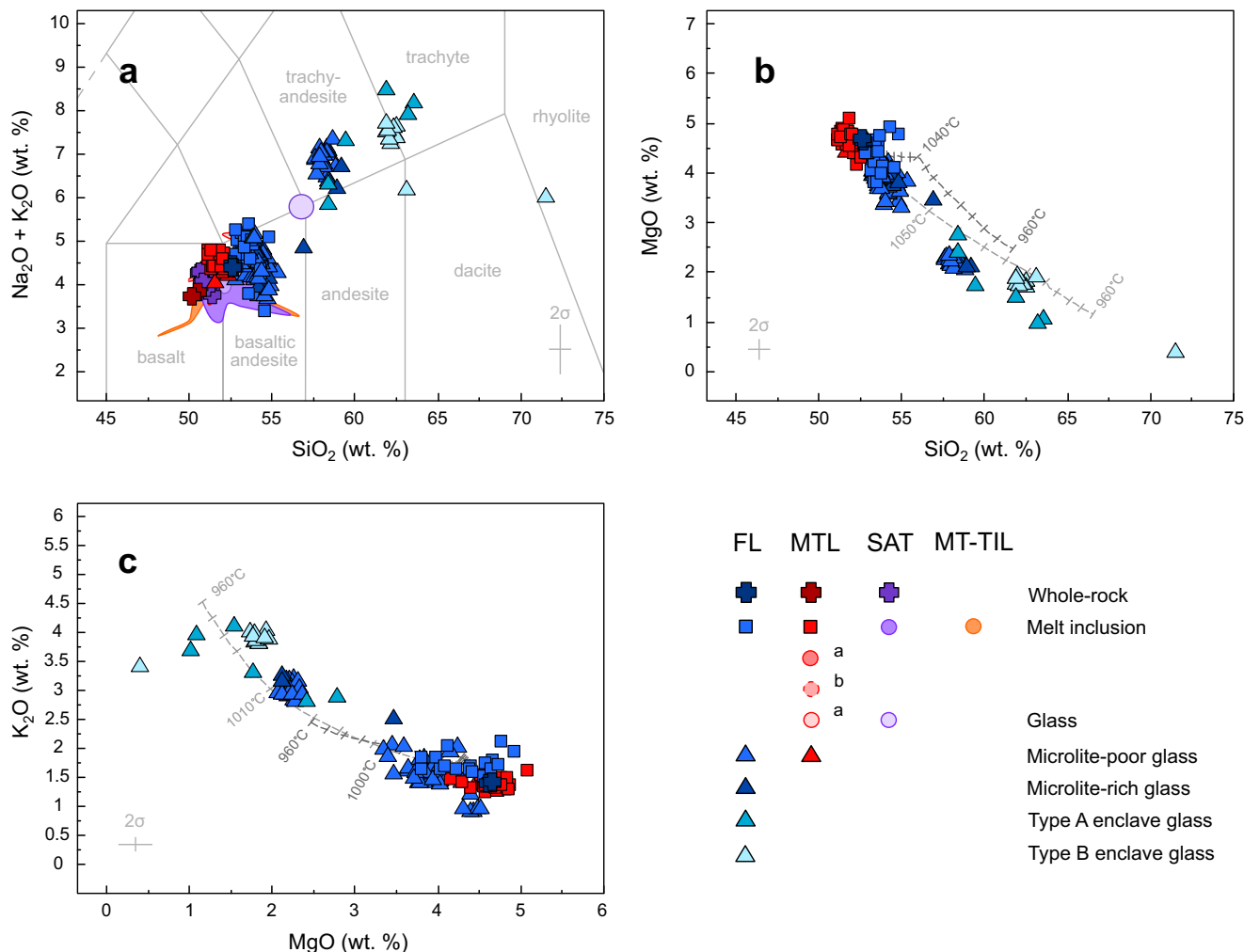


Fig. 3 Harker style diagrams illustrating the geochemical evolution of eruption products from Las Sierras-Masaya volcanic system. **(a)** A TAS plot illustrating the geochemical evolution of products sampled from a series of eruptions at Las Sierras-Masaya volcanic system. Accompanying the results from this study on the FL and MTL eruptions are additional whole-rock, MI and glass compositions of the MTL^{16,23}, SAT¹³ and MT-TIL²³ eruptions. For the MTL eruption, data from¹⁶ is indicated by ^a and data from²³ by ^b in the legend. **(b)** MgO vs SiO₂ and **(c)** MgO vs K₂O for whole-rock, MI, glass and enclave glass compositions in samples of the FL eruption. MI (red squares) and glass (red triangles) compositions of MTL samples from this study are also presented. MI from this study are PEC-corrected compositions. The liquid line of descent calculated by Rhyolite-MELTS³³ simulations is indicated by the grey dashed line, with tick marks representing an incremental temperature step of 10 °C, from 1080 to 960 °C, at a fixed pressure of 40 MPa and fO₂ of NNO-0.65. The dark-grey dashed line represents a liquid line of descent performed at a higher fixed pressure of 200 MPa, for the same temperature range and fO₂. Error bars represent the analytical uncertainty (2σ).

Our MI may have been affected by H⁺ diffusion, which may re-equilibrate H₂O concentrations. We selected MI from small, rapidly quenched scoriae 1–3 cm in size to minimise the effect of post-fragmentation H⁺ diffusion⁴³. H⁺ diffusion can occur prior to fragmentation at pre- and syn-eruptive conditions. The smallest MI closest to the rim of the smallest phenocryst hosts will be the most susceptible to diffusive loss of H₂O^{43,44}. Indeed, MI closest to the phenocryst rim show the lowest H₂O contents. However, these lower H₂O contents show some overlap with larger MI hosted in phenocryst cores, which would be less prone to diffusive H₂O loss. The short period of storage and rapid magma ascent may have limited the timescale for diffusive re-equilibration. FL MI likely experienced only minimal diffusive H₂O re-equilibration within the storage region, preserving the observed degassing trend. This exsolving vapour phase may have driven the ascent dynamics within the conduit, imparting increased buoyancy and gas pressure.

The Fontana Lapilli pre-eruptive condition. As mineral-melt thermometry is sensitive to melt H₂O concentration, we estimate pre-eruptive temperatures using the maximum H₂O content and the average H₂O content of 1.59 wt. % calculated from FL MI in this study and other works^{11,45}. Using the maximum H₂O content, we find matrix FL plagioclase phenocrysts and microlites crystallised within the temperature range 1050–1062 °C (Supplementary Fig. 2). The standard error of the Putirka⁴⁶ thermometer (Eq. 23) is ±43 °C. Pyroxene phenocrysts crystallised within the range 1063–1075 °C and microlites between 1051–1103 °C. The standard error of the Putirka⁴⁶ thermometer (Eq. 33) is ±45 °C. The majority of matrix less anorthitic plagioclase and pyroxene phenocrysts and microlites ($n_{\text{plg}} = 88/118$; $n_{\text{pyx}} = 11/11$) are in equilibrium with the average FL MI composition, using the equilibrium criterion of each thermometer. Our temperature range agrees with experimentally determined pre-eruptive conditions for the FL eruption of 40–80 MPa and 1010–1060 °C¹¹. Our estimated pressure range from Rhyolite-MELTS simulations (30–40 MPa) agrees with the lower end of this

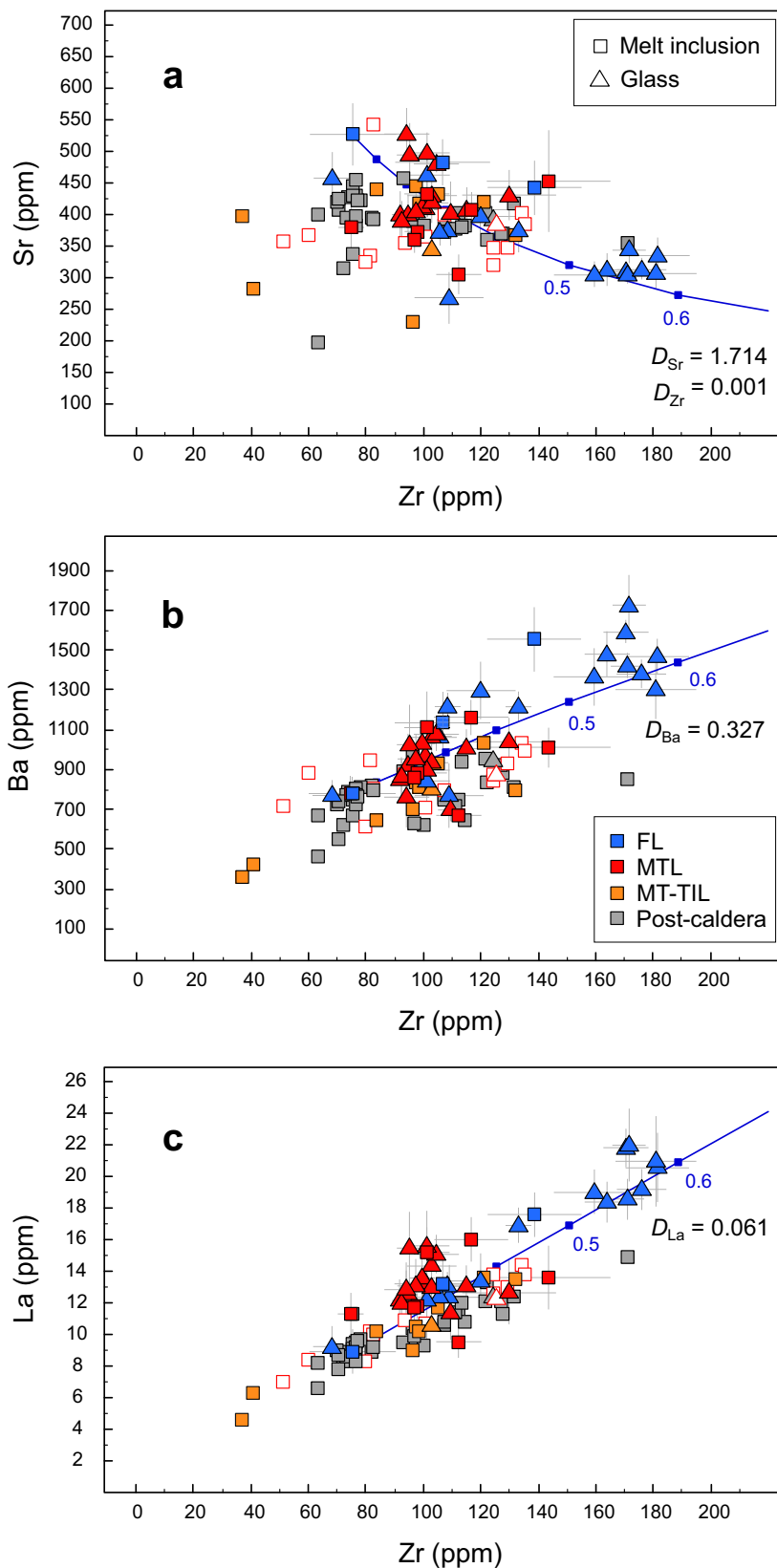


Fig. 4 Trace element concentrations measured in PEC-corrected plagioclase-hosted MI and matrix glass in samples of the FL eruption. Panels are presented in order of increasing incompatibility in plagioclase, from (a) Zr vs Sr, (b) Zr vs Ba to (c) Zr vs La. The melt differentiation trend for the FL eruption is modelled using the most primitive MI as the starting composition. Each square along the fractional crystallisation path represents an increase in crystal fraction of 0.1. Trace element concentrations in plagioclase-hosted MI and matrix glass of the MTL eruption are also presented. Literature data from samples of post-caldera activity^{20,23} and the MT-TIL eruption²³ are also shown. Literature data from samples of the MTL eruption²³ are highlighted by the open squares and triangles with the red outline. Grey error bars represent the analytical uncertainty (2σ) for samples from this study.

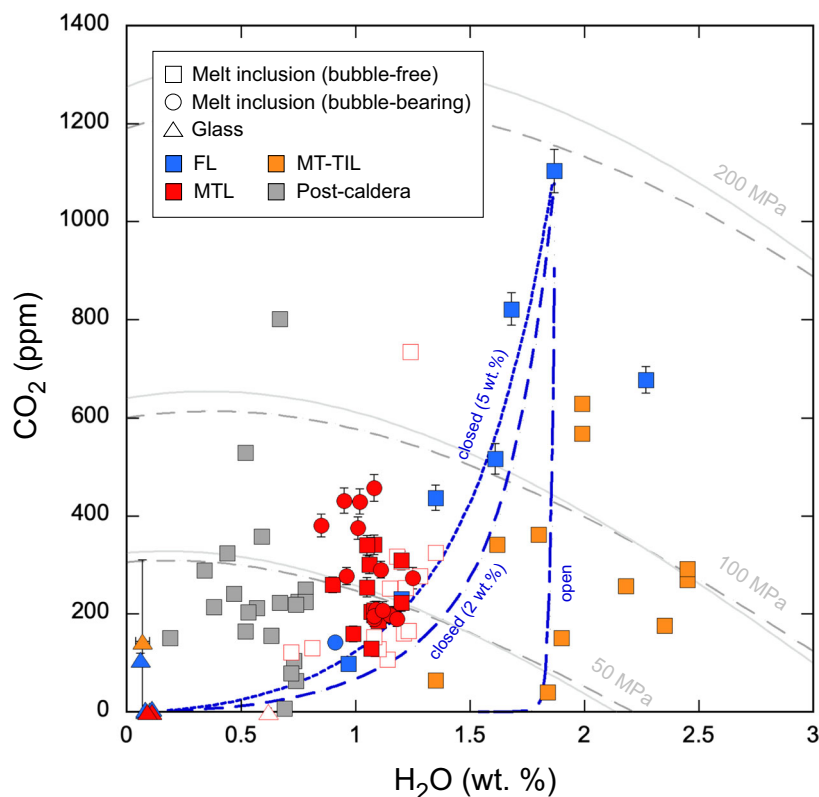


Fig. 5 PEC-corrected H_2O and CO_2 contents of MI and glass in samples of the FL and MTL eruptions. Bubble-bearing MI are represented by circles and bubble-free MI are represented by squares. Error bars represent the analytical uncertainty (2σ) for samples from this study. Grey lines show H_2O - CO_2 isobars modelled using MagmaSat⁴¹ at 50 MPa, 100 MPa and 200 MPa. The dark grey dashed lines show the isobars produced using the average MI composition of the FL eruption with temperature fixed at 1060 °C. The light grey lines show the isobars produced using the average MI composition of the MTL eruption¹⁶, with temperature fixed at 1100 °C. Closed and open system degassing trends modelled using MagmaSat⁴¹ are shown by the dashed blue lines, all modelled using a fixed temperature of 1060 °C. Closed system degassing trends are modelled in the presence of a range of exsolved volatile gas contents, expressed in wt. %. Literature data on the MT-TIL and MTL Plinian eruptions and from samples of more recent post-caldera activity²³ are also presented. The standard deviation of glass measurements for samples from Hlinka et al.²³ are indicated by the black lines (1SD).

experimentally determined pressure range¹¹. Costantini et al.¹⁰ find higher pre-eruptive temperatures of 1108–1130 °C for clinopyroxene crystallisation but used a lower input H_2O content for their thermometry calculations. Type A enclave plagioclase crystallised over a lower temperature range of 996–1006 ± 43 °C, and pyroxene between 988–1035 ± 45 °C. Type B enclave phases crystallised between 966–1036 °C. Enclave phases are in equilibrium with the average Type A and Type B enclave glass compositions respectively. Enclave crystals are small and euhedral and most likely crystallised towards the higher end of this range at low undercooling.

Using a lower H_2O content produces a higher calculated temperature for plagioclase (1076–1089 °C) and pyroxene (1060–1112 °C) phenocrysts and microlites. Type A enclave phases crystallise between 995–1044 °C and Type B phases between 973–1045 °C. However, calculated temperatures are still mostly <1100 °C.

Using the simulated output crystal fraction, measurements of phenocryst fraction ($\Phi_{\text{plg}} = 7$ vol.%; $\Phi_{\text{ol}} = 1$ vol.%; $\Phi_{\text{cpx}} < 1$ vol.%) and the results from mineral-melt thermometry^{16,36}, we find the FL magma that crystallised the matrix phases was last stored at pressures of 30–40 MPa and temperatures of 1050–1060 °C (Supplementary Data 2). The measured enclave crystal fraction can be reproduced at pressures of 30–40 MPa, but between 990 and 1000 °C. Textural observations, mineral-melt thermometry and geochemical modelling of melt evolution suggest that enclaves crystallised from a melt genetically related to that which crystallised the matrix phases but

represent a more prolonged stage of cooling and crystallisation. Enclave phases formed within the same pre-eruptive storage region as matrix phases but at an earlier point in time, crystallising in contact with their interstitial liquid and may be considered antecrystic⁴⁷. Unzoned, euhedral phenocrysts and microlites such as low-An plagioclase and pyroxene are in equilibrium with the average MI composition and can be considered autocrystic, forming from the last batch of melt prior to eruption⁴⁷. High-An plagioclase crystals are not in equilibrium with the average MI composition and may originate from deeper within the plumbing system as part of a second antecrystic crystal cargo injected into the magma chamber prior to eruption. However, it can be difficult to distinguish between autocrysts and antecrysts in mush-bearing systems due to the remobilisation of crystal cargo⁴⁷.

At depth, magma chambers likely do not exist as a single, continuous body of melt, but consist of crystalline mush and transient, eruptible melt lenses³². Cooling rates within the magma chamber would be greatest at the margin, where there is greater thermal contrast with country rock. Crystallisation would proceed first along the chamber walls and floor where magma temperatures are lower⁴⁸. Settling of crystals would occur towards the chamber floor⁴⁸. Numerical simulations of a shallow, differentiating, basaltic magma reservoir find convection transfers mass and heat, producing compositionally different liquids and temperature contrasts of several hundred degrees early within the reservoir's cooling history⁴⁸.

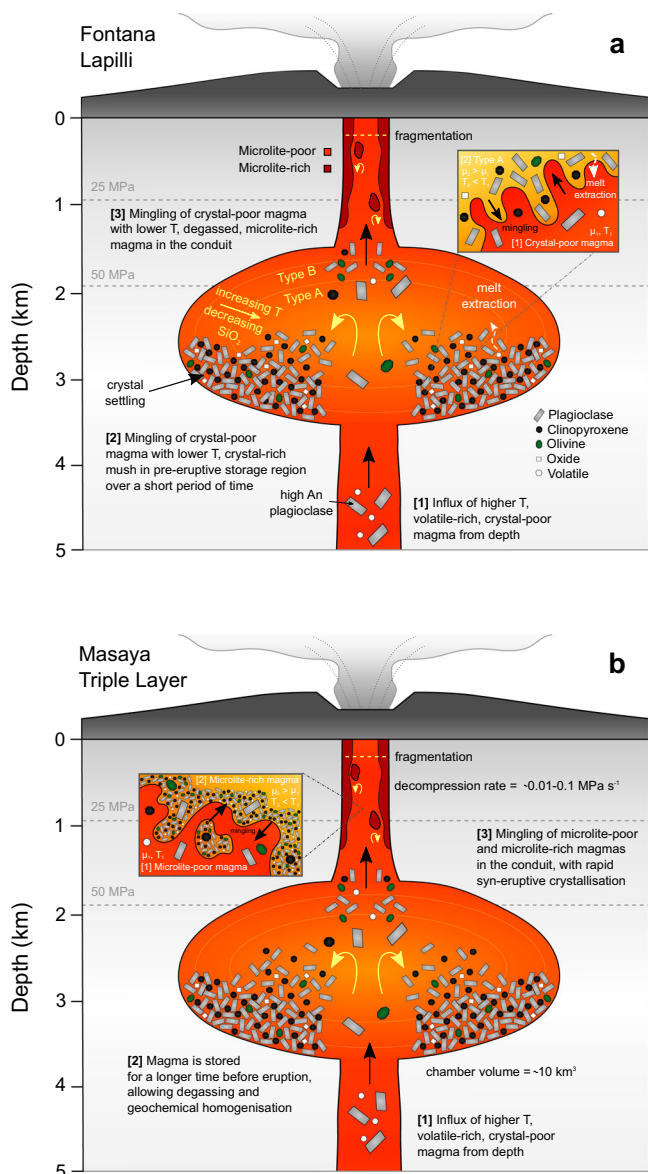


Fig. 6 A diagram illustrating the pre-eruptive condition of the FL and MTL eruptions of Las Sierras-Masaya volcanic system. For the (a) FL eruption, high-temperature (T), volatile-rich and crystal-poor magma from depth is injected into the shallow pre-eruptive reservoir, where it mingles with the lower temperature, crystal-rich mush in the storage region for a short period before eruption. Temperature contrast and crystal content is highest at the reservoir margin in contact with cooler host rock. Mush forming phases settle and accumulate along the reservoir floor. Convection transfers heat and mass within the reservoir. For the (b) MTL eruption, new magma injected from depth is stored for a longer period, allowing degassing and geochemical homogenisation within the storage region. This microlite-poor magma then mingles with the microlite-rich magma within the conduit, ascending at high velocities, with rapid syn-eruptive crystallisation in minutes enabling magma fragmentation within the conduit.

Crystallisation, assembly and mobilisation of crystal mushes can occur over days to months at basaltic systems^{49,50}. Crystal Size Distribution (CSD) calculations show enclave plagioclase could have crystallised within several days (Supplementary Fig. 3; Supplementary Table 2). CSD calculations provide a minimum residence time, as settling of mush-forming phases in the chamber is not considered. Crystallisation and volatile exsolution

could provide sufficient overpressure within the magma chamber to trigger an eruption^{36,51,52}.

We suggest that a batch of magma entered the reservoir, stagnating and crystallising a mush at the edge of the reservoir at temperatures of $\sim 1000-1040 \text{ }^\circ\text{C}$ and 30–40 MPa over several days. A fresh batch of volatile-rich, higher-temperature magma ($>1050 \text{ }^\circ\text{C}$) then entered the reservoir, where it was stored for only a short period of time at 30–40 MPa, crystallising a small plagioclase-dominated assemblage (Fig. 6). The addition of volatiles or higher-temperature melt into the intra-crystalline mush network likely induced melting and/or internal overpressure, unlocking the mush and enabling its eruption^{35,49}. The closed-system degassing trend modelled for the FL eruption suggests fresh magma intruding the reservoir was volatile-rich, providing overpressure within the sealed storage region that could trigger an eruption. As plagioclase-melt equilibrium is sensitive to melt H₂O content, disequilibrium between MI and their anorthitic hosts suggests that plagioclase hosts crystallised from a melt with a higher H₂O content within the deeper plumbing system, similar to the SAT, MTL and MT-TIL eruptions^{13,23}. FL MI which record entrapment pressures $>40 \text{ MPa}$ may represent the volatile-rich magma injection originating from greater depth. These MI may have had insufficient time to re-equilibrate during the short storage time within the shallow reservoir, preserving higher volatile concentrations and entrapment pressures.

Comparison with other eruptions of Las Sierras-Masaya volcanic system. We compare our FL pre-eruptive scenario with the SAT and MTL eruptions. SAT MI have low H₂O contents of 1.03–2.22 wt.%¹³, comparable to FL MI contents. Similarly, SAT samples show both basaltic-basaltic andesitic and andesitic glass. Pérez et al.¹³ calculated that the SAT andesitic matrix glass (Fig. 3a) can be produced by crystallisation of 25% plagioclase, 15% clinopyroxene, 3% olivine and 5% magnetite, comparable to our measured enclave crystallinity (Supplementary Table 1). The SAT andesitic glass is interpreted as a residual melt from crystallisation and differentiation of a batch of SAT basaltic magma at the reservoir walls, consistent with our FL pre-eruptive condition. Although cumulates were not observed in SAT samples, the andesitic magma indicates cooling, crystallisation and melt differentiation within the storage reservoir, producing a glass composition comparable to our FL enclave glass¹³.

MTL samples also show microtextural heterogeneity¹⁶ (Fig. 2b–d). However, there is minimal evolution concerning MTL major (Fig. 3a) and trace element geochemistry (Fig. 4). Compared to FL MI, a narrower range of 0.85–1.25 wt.% H₂O and 129–457 ppm CO₂ is measured in MTL PEC-corrected MI (Fig. 5). Our results for the MTL eruption are comparable to Hlinka et al.²³, but are lower than the maximum H₂O content of 2 wt.% measured for MTL MI using Raman spectroscopy¹⁶. The small size of some MTL MI may indicate that they were susceptible to diffusive H₂O loss, despite the small size of scoriae⁴³. Diffusive re-equilibration may have produced the low MTL MI H₂O contents. Higher H₂O contents of 5–6 wt.% H₂O have been suggested for the SAT, MTL and MT-TIL eruptions^{13,23}. MI then experienced re-equilibration of H₂O during a short storage period within the shallow reservoir^{13,23}. Thus, the homogeneous H₂O contents measured in MTL MI most likely represent the magmatic conditions prior to eruption.

Calculated MTL MI entrapment pressures range between 33–83 MPa, but most cluster at lower values. As we measure only the MTL MI glass phase, reported CO₂ contents and calculated entrapment pressures represent minima. We observe only a small variation comparing the glass CO₂ content of bubble-bearing (54% of MTL MI) and bubble-free MI, suggesting negligible CO₂

loss to vapour bubbles, consistent with previous work²³. Our maximum measured CO₂ content of 457 ppm is consistent with previous work which finds that most CO₂ contents do not exceed 400 ppm for the MTL, MT-TIL and recent eruptions²³.

FL MI cluster at the lower end of H₂O and CO₂ contents, with entrapment pressures <100 MPa. However, FL MI record higher entrapment pressures than MTL MI within the most primitive MI (Supplementary Fig. 4). The preservation of a degassing trend and a wide range in volatile contents in FL MI suggests that the FL magma was stored for less time than the MTL magma, limiting the extent of degassing and homogenisation of melt compositions. A more prolonged period of storage and pre-eruptive degassing for the MTL eruption may have produced the invariant, lower MI volatile concentrations and homogeneous melt chemistry, obscuring any original degassing trend (Fig. 6). Storage within the shallow reservoir, degassing and fractionation at Masaya has produced geochemically homogeneous erupted products over time^{20,22}. The FL and SAT basaltic-andesitic and andesitic glass suggests that these magmas were stored for shorter durations at shallow depth compared to the MTL and MT-TIL magmas.

Evidence suggests that the Las Sierras-Masaya magmas were stored within a reservoir at shallow depth (<4 km) prior to eruption, degassing and crystallising the mineral assemblage^{13,16,20,22,23}. Magma stagnation and degassing at shallow crustal depth is suggested as a consistent pre-eruptive stage at Masaya regardless of eruptive style, producing the low volatile contents of Masaya MI²³. Our pre-eruptive scenario for the FL eruption is consistent with this model.

The FL eruption had the lowest pre-eruptive temperature of the Las Sierras-Masaya Plinian eruptions. The more recent Plinian eruptions show higher pre-eruptive temperatures of 1075–1161 °C (SAT), 1080–1100 °C (MTL) and 1080 °C (MT-TIL)^{13,16}. Cooling within the magma reservoir can lead to crystallisation of a mush, as observed for FL samples. Back-scattered electron (BSE) images of MTL enclaves suggest inclusions of mush may have been erupted (Supplementary Fig. 5).

The transition from steady-state open conduit activity to a Plinian eruption is suggested to be modulated by sealing of the conduit, producing a closed system and build-up of overpressure²³. We suggest that cooling and crystallisation of a mush at shallow crustal depth could provide a mechanism for sealing the system. The mush, together with the injection of volatile-rich magmas into the storage region, may contribute to the increase in overpressure of the system and assist in unlocking the mush³⁵ (Fig. 6). Therefore, the eruptive style at Las Sierras-Masaya volcanic system is closely related to the initial, pre-eruptive conditions. Although brittle magma fragmentation is most likely driven by syn-eruptive microlite crystallisation and restricted outgassing within the conduit^{15,16}, the initial, pre-eruptive conditions may promote this scenario by producing a lower temperature, higher viscosity magma more susceptible to fragmentation within the conduit. The relative importance of these initial conditions and their control on eruptive style can be investigated using numerical modelling.

Conduit dynamics of a basaltic Plinian eruption. We used the 1D, multiphase, steady-state conduit model of La Spina et al.^{25–27} to simulate a basaltic Plinian eruption at Masaya caldera. The governing equations driving the multiphase flow are those illustrated in La Spina et al.²⁷ and for completeness have been reported in the Supplementary Methods. The constitutive equations needed to characterize the magma ascent dynamics at Masaya caldera are described in the Methods section. The initial

conditions (Supplementary Table 3) are informed by the results of this study and Bamber et al.¹⁶. The maximum measured MI CO₂ content from this study is used as the initial dissolved CO₂ concentration. Initial pressure, temperature, crystal content and dissolved H₂O concentration values are from Bamber et al.¹⁶. We use the strain-rate criterion of Papale⁵³ to simulate fragmentation, where failure occurs when the Deborah number exceeds 0.01⁵³. We set the characteristic time of crystallisation to 10 s, consistent with previous work on the Etna 122 BCE Plinian eruption¹⁵.

Our reference simulations focus on characterising the MTL conduit dynamics. The MTL pre-eruptive conditions likely represent the current system and future possible Plinian activity. The MTL vent location is thought to lie within the present-day Masaya caldera, whereas the FL vent location is not well known but thought to lie outside the modern caldera². The FL crystal cargo, with fragments of mush, makes it difficult to assign an initial crystal content and to describe the syn-eruptive crystallisation process. Instead, the FL pre and syn-eruptive conditions constrained by this study are explored through a sensitivity analysis.

We address the rheological behaviour of the heterogeneous magma by defining two endmembers from natural observations: a microlite-poor and microlite-rich case (Fig. 2b–d). Here, crystal-poor and crystal-rich simulations refer to the microlite-poor and microlite-rich endmembers defined from observations, as we do not consider enclaves within our simulations. We vary the initial conditions until the output reproduces the observed crystal content in our samples, which we take as representative of the crystal content at the vent. The initial crystal fraction (ϕ) and the initial pre-eruptive temperature (T) differ between the crystal-poor ($T = 1090$ °C; $\phi = 10$ vol. %) and crystal-rich ($T = 1070$ °C; $\phi = 17$ vol. %) simulations. The initial temperatures agree with the estimated MTL pre-eruptive temperature range, accounting for the standard error of mineral-melt thermometry¹⁶. The initial crystal fraction of the crystal-poor endmember agrees with the observed MTL phenocryst fraction. Although the crystal-rich endmember is produced using a higher initial crystal fraction, the agreement between the output crystal fraction and microtextural observations indicates a higher crystal fraction may have been needed to produce the crystal-rich endmember. The crystal-poor simulation (Fig. 7, solid lines) produces a total exit crystal fraction of 0.24, and the crystal-rich simulation (Fig. 7, dashed lines) a total fraction of 0.51, comparable with the measured crystal fractions for the microlite-poor and microlite-rich regions in MTL samples of Plinian phase TLL2¹⁶.

The crystal-poor simulation produces an effusive eruption, as the critical Deborah number is not reached during magma ascent (Fig. 7a) and there is no fragmentation within the conduit. For the crystal-rich simulation, fragmentation occurs ~280 m below the vent (Fig. 7a). Syn-eruptive crystallisation in the crystal-rich simulation drives a considerable increase in mixture viscosity (Fig. 7b), reaching the critical Deborah number for fragmentation. The lower viscosity, crystal-poor endmember (Fig. 7b) enters the conduit at a higher velocity on the order of 10 m s⁻¹ (Fig. 7c), producing a higher mass flow rate of 1.1 × 10⁸ kg s⁻¹ (Fig. 7d). The higher viscosity crystal-rich endmember enters the conduit at lower velocity on the order of 1 m s⁻¹, resulting in a lower mass flow rate of 6 × 10⁶ kg s⁻¹. Gas-melt coupling is maintained during ascent for the crystal-poor endmember and prior to fragmentation for the crystal-rich endmember (Fig. 7c). Both mass eruption rates lie within the range in mass eruption rate of 10⁶–10⁸ kg s⁻¹ indicated by the MTL deposit³. The average decompression rate is 0.91 MPa s⁻¹ and 0.05 MPa s⁻¹ for the crystal-poor and crystal-rich simulations respectively. Our simulated decompression rates are comparable to estimates of the

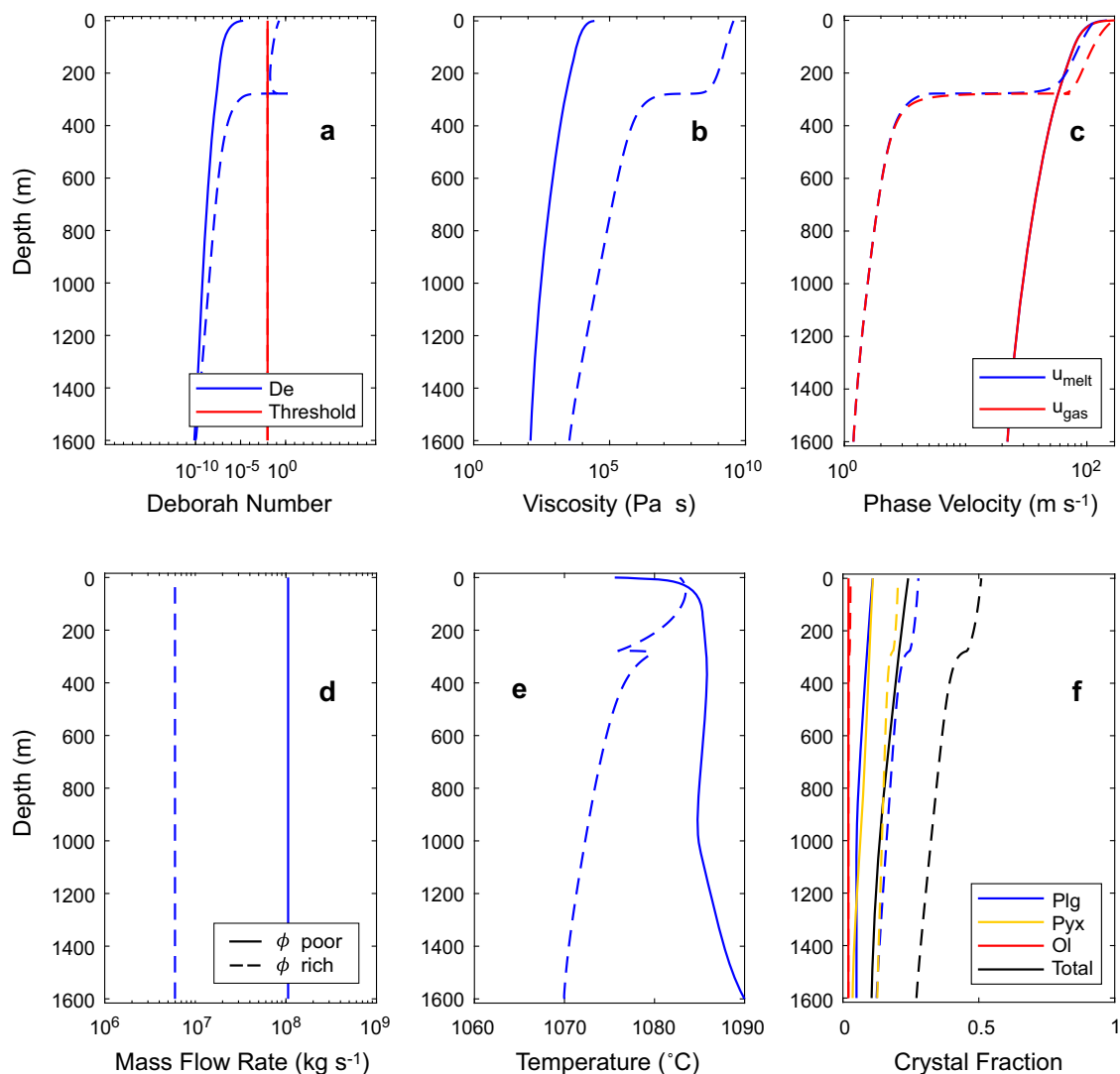


Fig. 7 Numerical solutions using the conduit model for the Masaya Triple Layer eruption. Results for the crystal-poor endmember are indicated by solid lines, and results for the crystal-rich endmember are highlighted by dashed lines. **(a)** Deborah number, **(b)** viscosity, **(c)** phase velocity (u), **(d)** mass flow rate, **(e)** temperature and **(f)** crystal fraction. For **(c)**, u_{melt} and u_{gas} overlap until fragmentation occurs as the gas and melt phases are coupled and ascend with the same velocity. For the crystal-poor endmember u_{melt} and u_{gas} continue to overlap as fragmentation does not occur. For the crystal-rich simulation, the Deborah number is reached at ~280 m below the vent and magma fragmentation occurs. The increase in crystal fraction and consequently magma viscosity during magma ascent leads to fragmentation for the crystal-rich simulation. Both simulations have an initial depth of 1600 m, corresponding to the depth of the magma reservoir.

FL decompression rate from experiments and calculations using bubble number densities, which are on the orders of 0.1 and 1 MPa s^{-1} respectively^{12,54}.

The rapid ascent velocity results in a short ascent time, between 1–13 min considering both endmember simulations. The calculated timescale is consistent with CSD analysis of the MTL samples, which suggests rapid syn-eruptive crystallisation within minutes during magma ascent¹⁶. Experiments demonstrate that rapid syn-eruptive crystallisation can occur within minutes at high undercooling, driving basaltic magma fragmentation during ascent¹⁵. The lower initial temperature of 1070 °C for the crystal-rich simulation provided a higher undercooling, facilitating rapid crystallisation and magma fragmentation. The temperature of the crystal-rich simulation increases during magma ascent due to the release of latent heat of crystallisation. The amount of latent heat produced by syn-eruptive crystallisation exceeds the decrease in temperature produced by adiabatic cooling during ascent, which is instead observed for the crystal-poor simulation.

Heterogeneous textures can reflect portions of the same initial magma that experienced different extents of microlite crystallisation⁵⁵. Microlite-rich domains are expected to experience a more extended period of crystallisation, ascending at lower velocities and in cooler zones of the conduit⁵⁵. A 40 °C decrease in the temperature of crystallisation may have produced crystalline tachylite glass as opposed to sideromelane during the 2001 CE Etna flank eruption⁵⁶. Our simulations demonstrate the two endmembers defined from natural observations can be produced by decreasing the initial temperature by 20 °C and increasing the initial crystal content by 7 vol.%. With a small change in temperature and initial crystal content (Fig. 7e, f), a large microtextural difference can be produced during magma ascent. This result suggests that the two textural endmembers can be produced from a small difference in initial conditions, which then experience different degrees of syn-eruptive crystallisation during ascent. This difference in crystallisation produces a large viscosity contrast between the endmembers of 10^4 – 10^7 Pa s .

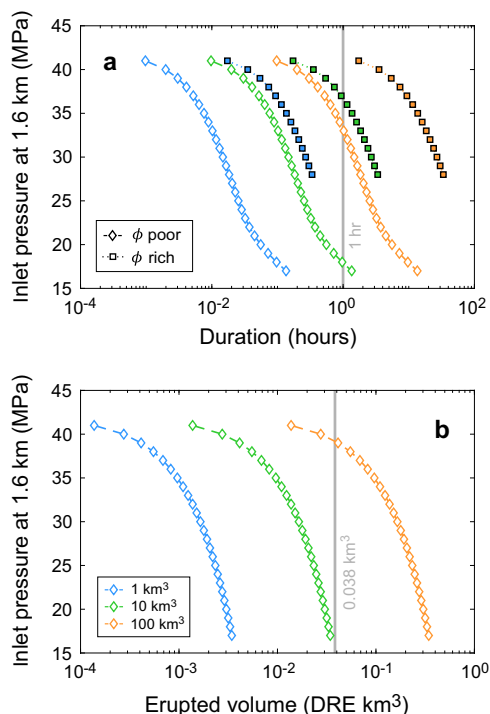


Fig. 8 Variation in eruption duration and erupted volume with inlet pressure for different chamber volumes for Plinian phase TLL2 of the MTL eruption. Results for the crystal-poor endmember are shown by the open diamonds, and results for the crystal-rich endmember are shown by the filled squares for the variation in (a) eruption duration and (b) erupted volume with inlet pressure. The duration and erupted volume of Plinian phase TLL2 calculated by Pérez et al.³ (phase II) are shown as grey bars. In (b) we plot only the results of the crystal-poor simulations, as those of the crystal-rich simulations are coincident, but instead the final crystal-rich simulation corresponds to an inlet pressure of 28 MPa. The crystal-poor and crystal-rich simulations are coincident as a result of Eq. (4), where the erupted volume depends on the properties of the magma chamber and δp_{ch} , which are fixed for a given simulation.

We use the magma ascent model to estimate the magma reservoir volume that supplied the MTL eruption. We find calculations using a chamber volume of 10 km³ are consistent with the duration (~1 hr) and the minimum erupted volume (0.038 km³ DRE) estimated from land outcrops of MTL Plinian phase II³, where the duration is estimated from the mass flux and erupted mass of the deposit (Fig. 8). The total MTL erupted volume is ~2 km³ (DRE) considering offshore deposits¹³. The rate of magma flux into the present-day Masaya reservoir has been estimated at ~0.19 km³ yr⁻¹²⁰. Using our chamber volume estimate of 10 km³, the volume of the Plinian eruptions will have accumulated within a minimum of ~50 years. Although mush may crystallise rapidly at Masaya, a critical crystal fraction may need to be reached within the reservoir for incoming, volatile-rich fresh magma to generate sufficient overpressure to trigger the eruption. As crystallisation likely proceeds from the reservoir margin, it may take years to assemble a magma volume capable of producing a Plinian eruption.

Sensitivity analysis. We perform a sensitivity analysis to identify the most important parameters driving explosive and effusive activity at Las Sierras-Masaya volcanic system and their effect on output parameters such as mass eruption rate, exit velocity, total crystal content and mixture viscosity. We selected a range of values for the input parameters which incorporate the pre-

eruptive conditions determined for the eruptions of Las Sierras-Masaya volcanic system. We use our constraints on initial temperature, crystal content, and dissolved H₂O and CO₂ from this study for the FL eruption. Our sensitivity analysis uses the average MTL MI composition, which we assume is representative of the melts being delivered to Masaya's shallow magma chamber due to the compositional homogeneity of erupted products through time²⁰.

Explosive solutions (Fig. 9a–j, square symbols) occur when the critical Deborah number is reached, resulting in brittle magma fragmentation. In our sensitivity analysis, <20% of solutions are explosive, consistent with the rarity of highly explosive eruptions at this system. Non-explosive solutions (Fig. 9a–j, diamond symbols) represent a wider range in eruptive style²⁷, which we define using the average exit velocity (represented by the colour of the diamond symbols). Model solutions for which the fragmentation threshold is not reached, but exit the vent at a high ascent velocity, likely represent lava fountaining activity²⁷. Lava fountain activity is expected to occur when exit velocities exceed 1 m s⁻¹ for low fountain activity (jet height is 0.1–50 m) and 30 m s⁻¹ for high fountain (jet height >50 m) activity²⁷. Non-explosive solutions with a lower exit velocity likely represent effusive eruptions such as lava flows. As we adopt a small characteristic time of crystallisation, we may overestimate the number of explosive solutions¹⁵.

The initial temperature has a strong control (Fig. 9a) on the frequency of explosive vs. non-explosive solutions (Supplementary Fig. 6a). As initial temperature decreases from 1100 °C, the frequency of explosive solutions increases, reaching a maximum of 80% at temperatures of 1060 °C, due to the increase in melt viscosity with decreasing temperature and the control of temperature on syn-eruptive crystallisation (Supplementary Fig. 6b). Following this trend, we can infer that at lower temperatures the percentage of explosive simulations would exceed 80%.

There is a positive correlation between increasing temperature and the frequency of non-explosive solutions. Only non-explosive solutions are observed at temperatures exceeding ~1100 °C. This result agrees with the FL and MTL pre-eruptive temperatures of <1100 °C constrained by mineral-melt thermometry¹⁶. Combining these results, we suggest that a low pre-eruptive temperature may have been a driving cause of Plinian activity at this volcanic system. The decrease in exit velocity with decreasing temperature indicates that a transition from high-velocity to low-velocity effusive activity may signify a future shift to explosive activity.

The conduit radius has minimal influence on the relative frequency of explosive/non-explosive solutions (Fig. 9c) but exerts a control on the mass flow rate (Supplementary Fig. 6c). As a high mass eruption rate is required to produce a sub-Plinian to Plinian eruption (10⁶–10⁸ kg s⁻¹), we expect most explosive solutions of Plinian magnitude to occur at larger values of the conduit radius. The increased frequency of Plinian activity at Masaya following the SAT eruption may be attributed to the SAT eruption establishing a larger conduit radius. Following the MT-TIL eruption, activity has been largely controlled by the fault structures remaining from caldera formation and the extensional stress exerted by the Managua graben. The 1772 CE lava flow was erupted from a fracture linked to the Cofradías fault⁵⁷.

The sensitivity analysis shows a small increase in the frequency of explosive solutions between H₂O contents of 1 and 1.5 wt.% as volatile-saturated conditions are approached (Fig. 9d). The frequency of non-explosive eruptions increases in water undersaturated conditions. Once water-saturated conditions are exceeded (~1.5 wt.% H₂O), the frequency of explosive eruptions slightly decreases with increasing H₂O content. These results suggest that high H₂O concentrations may not be required to

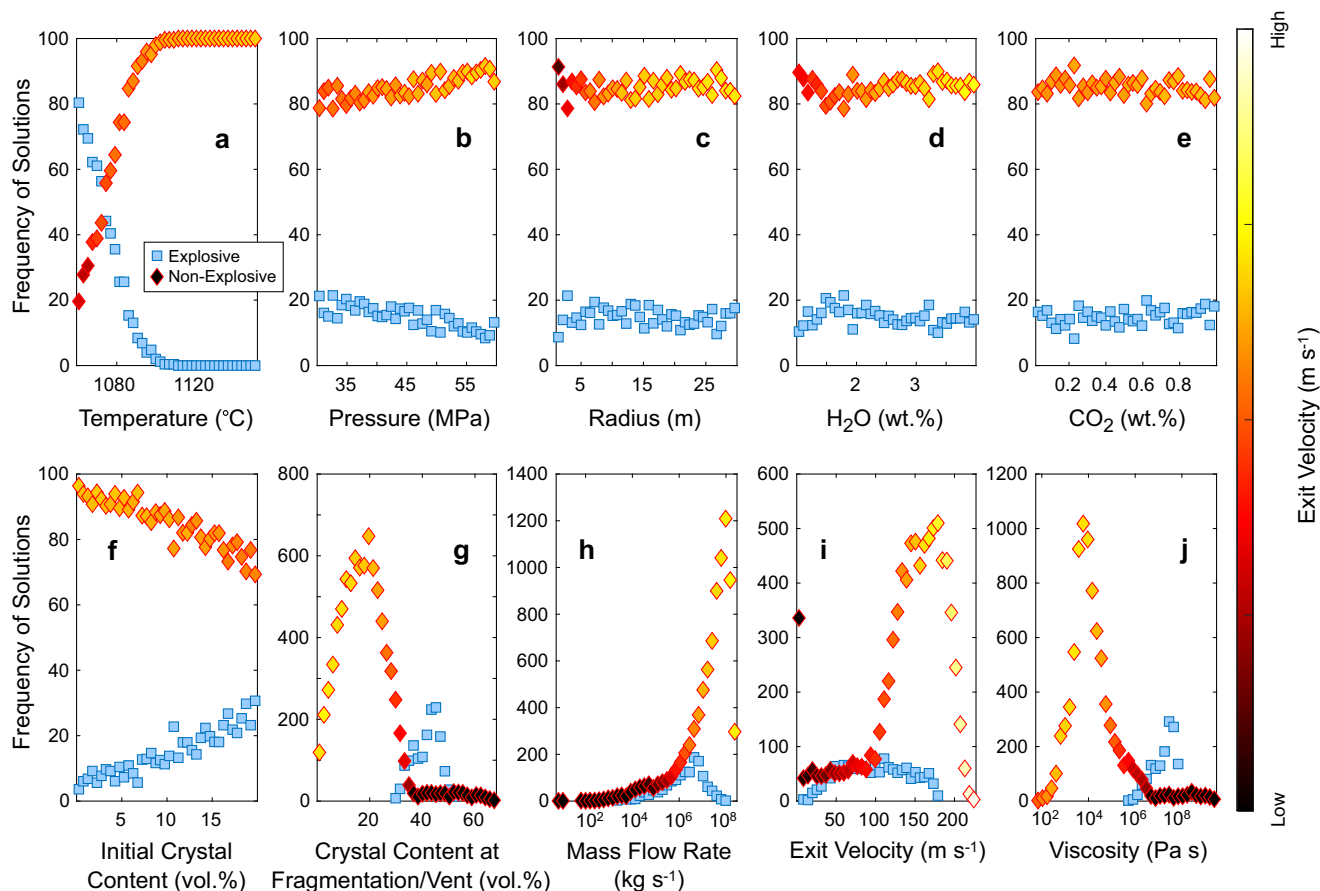


Fig. 9 Results of the sensitivity analysis. Explosive solutions are shown in blue. Non-explosive solutions are coloured according to average exit velocity, according to the colour bar. The frequency of solutions is plotted against the input parameters **(a)** initial temperature, **(b)** initial pressure, **(c)** conduit radius, **(d)** initial H₂O concentration, **(e)** initial CO₂ concentration, and **(f)** initial crystal content. Results are plotted as the number of solutions, but for the input parameters **(a–f)** the sum of the frequencies is 100, and therefore these results are expressed as a percentage. Also presented are the frequency of solutions plotted against output parameters **(g)** crystal content at fragmentation (for explosive solutions) and at the vent (for non-explosive solutions) **(h)** mass flow rate, **(i)** exit velocity, and **(j)** viscosity, at fragmentation for the explosive case, and at the vent for the non-explosive case. For the output parameters **(g–j)** the sum is variable and expressed as the raw total.

produce a Plinian eruption at this system, but only sufficient H₂O to establish volatile-saturated conditions. Magmas stored at shallow crustal depth may be able to erupt explosively if volatile-saturated conditions are reached. The maximum measured MTL pre-eruptive H₂O content¹⁶ agrees with these results.

High initial CO₂ concentrations have been implicated as a driving mechanism of explosive basaltic activity^{58,59}. Even if our measurements of MI CO₂ represent minima, the sensitivity analysis results show that the frequency of explosive solutions is not particularly sensitive to the initial CO₂ content, even up to 10,000 ppm (Fig. 9e). Our measurements and numerical simulations suggest high initial volatile concentrations were not a critical condition promoting Plinian activity at this volcanic system.

The frequency of explosive solutions increases with increasing initial crystal content (Fig. 9f), due to the increase in mixture viscosity. We can assume that enclaves would increase the likelihood of an explosive eruption. Numerical results show explosive solutions start to occur when the total crystal content exceeds 30 vol.%, as a higher crystal content will increase mixture viscosity (Fig. 9g). FL, MTL and MT-TIL samples show high crystal contents, between 48 and 64 vol.%^{10,16,23}. Instead, present-day lava lake ejecta shows low microlite contents of 5 vol.%²³.

The exit velocity and the degree of gas-melt coupling show a relationship with eruptive style (Fig. 10). Numerical results show that at high values of Reynolds number (>10²) and low viscosity

(<10⁴ Pa s) magma is not able to fragment within the conduit and exits the vent at high speed (on the order of 10–10² m s⁻¹), producing lava fountaining activity²⁷. At higher viscosity (between 10⁵ and 10⁸ Pa s), the exit velocity decreases and both explosive and effusive activities become more likely. Results show that a strong coupling between gas and melt is not required to produce an explosive eruption, in agreement with La Spina et al.²⁷. As the viscosity increases even further (>10⁸ Pa s), magma ascent rate continues to decrease, and gas can decouple efficiently from the melt, preventing the formation of high strain rates, and thus producing only effusive eruptions.

Although we account for the heterogeneity of the MTL magma by defining two endmembers in our simulations, we recognise that there could be a complex, nonlinear behaviour during magma ascent. The effect of the two intermingling endmembers and their relative contribution to bulk mixture viscosity is difficult to constrain. In a magmatic system, the mass eruption rate and viscosity ratio between the two endmembers can control the development of instabilities and physical mixing^{60,61}. The viscosity ratio between the endmembers is expected to be large due to their differences in temperature and crystallinity¹⁶, where viscosity increases from 10² to 10⁶ Pa s. Future work investigating the impact of the physical mixing of two endmembers with different crystallinities on bulk mixture viscosity is needed. For our simulations, the large viscosity ratio between the

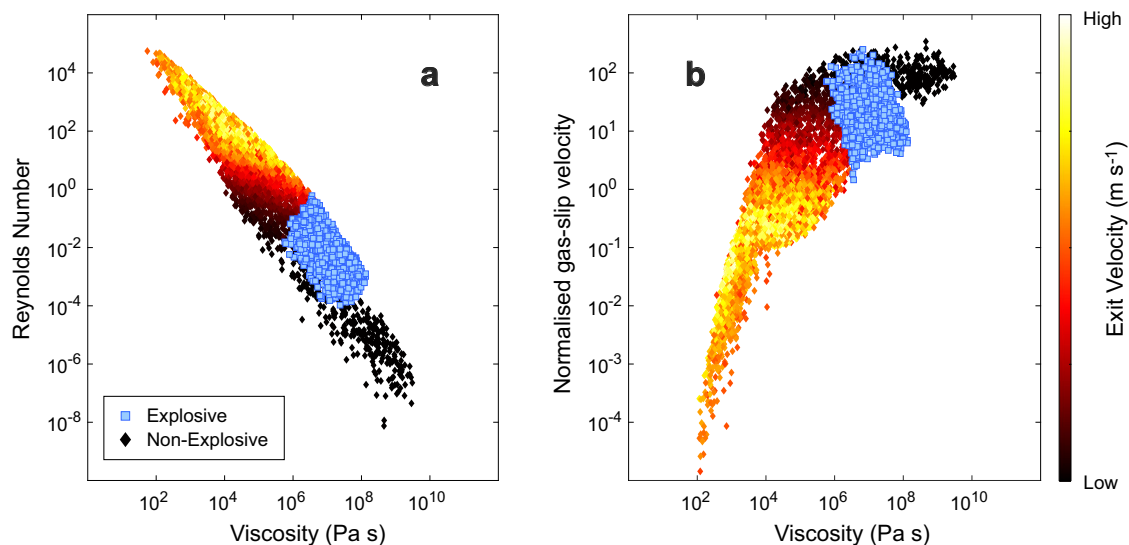


Fig. 10 Plots showing the correlation between output parameters, obtained from the sensitivity analysis. The correlation between viscosity and (a) Reynolds number and the (b) normalised gas-slip velocity is shown. Explosive solutions are shown by the blue squares. Non-explosive solutions are shown by the diamonds, coloured by exit velocity. For the explosive solutions, all parameters represent the value at fragmentation, whilst for the non-explosive solutions, all parameters represent the value at the vent. In (b) gas-slip velocity is normalised by melt velocity.

endmembers should produce turbulent flow, enabling efficient syn-eruptive mingling in the conduit⁶¹ but not sufficient to homogenise the two endmembers, preserving the heterogeneous textures observed in the samples.

Low-viscosity basaltic systems such as Kilauea rarely produce explosive eruptions without external water²⁷. A numerical investigation found that the range of pre-eruptive conditions at Kilauea, with temperatures ~ 1150 °C, crystal contents < 5 vol.% and H₂O contents < 1 wt.%, are not favourable to explosive eruptions, instead producing fountaining activity²⁷. The Las Sierras-Masaya magmas are lower temperature, more crystalline and have a higher volatile content. They are therefore more likely to be higher viscosity. Although pre-eruptive temperatures for recent and Plinian activity at Masaya can overlap, there is a tendency for samples of recent activity to reach pre-eruptive temperatures which exceed 1100 °C²³.

Conclusion: Pre- and syn-eruptive conditions of basaltic Plinian eruptions. To draw a complete picture of the conditions promoting basaltic Plinian volcanism, we compare our constraints on pre- and syn-eruptive conditions from Las Sierras-Masaya volcanic system with other basaltic Plinian eruptions (Supplementary Table 4). The Las Sierras-Masaya, Etna and Tarawera Plinian eruptions show pre-eruptive temperatures < 1100 °C. Low pre-eruptive temperature was likely a fundamental condition to achieve high undercooling during magma ascent, rapid crystallisation, and brittle magma fragmentation¹⁵, evidenced by the high microlite crystal fractions observed in the Etna 122 BCE and Tarawera samples^{8,9}. From our sensitivity analysis, we find that a critical condition for an explosive Plinian eruption is a pre-eruptive temperature < 1100 °C and total crystal content > 30 vol.%, in agreement with Arzilli et al.'s¹⁵ predictions for the Etna 122 BCE Plinian eruption. Cooling, crystal-rich basaltic magma may accumulate in mush-bearing systems such as Etna, which show a wide range in explosive activity⁶².

The Las Sierras-Masaya and Etna 122 BCE Plinian eruptions shows similar volatile concentrations, suggesting that lower initial volatile concentrations are sufficient to drive a basaltic Plinian eruption. However, a free fluid phase may have also driven the ascent dynamics of the FL and Etna 122 BCE eruptions⁶³. Similar

to the FL eruption, crystallisation, closed system degassing and accumulation of volatiles within the uppermost storage region is expected to have occurred prior to the Etna 122 BCE eruption⁶³. However, CO₂ fluxing and open system degassing also characterised ascent of the Etna 122 BCE magma from the deeper plumbing system⁶³. Sub-Plinian to Plinian eruptions show fast decompression rates (0.1 – 0.2 MPa s⁻¹) and rapid ascent rates (> 10 m s⁻¹) within the conduit, indicating that rapid decompression and ascent provided little time for gas-melt separation (Fig. 7c), even within short conduits such as those of Masaya and Sunset Crater^{12,64}. Therefore, there may be limited time between the onset of potential precursory activity and eruption.

Although the last Plinian eruption of Las Sierras-Masaya volcanic system occurred ~ 1800 years ago, multiple episodes of Plinian activity suggests that under the right conditions, there could be a sudden transformation to a highly explosive system. Changes in the pre-eruptive system could be identified through examining micro-textures of erupted products, which may show crystalline enclaves indicative of processes occurring at depth such as formation of a mushy magma; monitoring changes in gas geochemistry to identify the arrival of fresh, volatile-rich magma; or monitoring deformation and seismic signals to identify possible inflation or deflation following changes in the storage region. As large magma volumes can assemble at Masaya within 50 years, the explosive transition could occur rapidly. As these conditions are shared with other basaltic Plinian eruptions, cool storage of crystal-rich basaltic magma at shallow depth may be a crucial pre-eruptive condition driving highly explosive and hazardous eruptions at basaltic volcanoes.

Methods

Sampling. Samples of the FL eruption are 1–3 cm sized scoriae, taken from units A/B to lower G (LG) 2. We use the same nomenclature for our samples, where FonD refers to unit D of the FL deposit. Samples are taken from proximal sites $12^{\circ}03'18.4$ °N, $86^{\circ}14'38.2$ °W and $12^{\circ}01'36.9$ °N, $86^{\circ}15'00.1$ °W (Fig. 1). Samples of the MTL eruption are from the same location as Bamber et al.¹⁶.

Major and trace element analysis. Homogenised glass chips were prepared for whole-rock compositional analysis at the Department of Physics and Geology, Università degli studi di Perugia, Italy, due to the presence of enclaves. Scoriae of units A/B and E of the FL eruption were crushed to a fine powder and heated within a crucible until melted. This melt was then rapidly quenched in air on

removal from the furnace. Glass chips were homogenous and crystal-free. Glasses were mounted in epoxy resin and polished. For major and trace element analyses of glasses and minerals, scoriae (A/B to LG for the FL samples and MTL_L2 for the MTL samples) were mounted as 300 µm thick wafers on glass slides and polished.

Electron probe microanalysis (EPMA) was conducted using the JEOL JXA-8530F FEG electron microprobe at the Photon Science Institute, University of Manchester, to determine major element chemistry of seven FL samples. BSE images of sample textures were also acquired using the same instrument. BSE images were used to inspect MI prior to EPMA analysis and visibly crystallised inclusions were not analysed. We used a dual condition set-up to measure both crystals and glasses whilst minimising potential devolatilisation of the glass. The operating conditions for analysis of crystals were: an acceleration voltage of 15 kV, a beam current of 7–10 nA and beam diameter of 1–5 µm. For the analysis of glasses, the beam current was reduced to 2–7 nA and the beam diameter increased to 5–15 µm. Peak count times for all elements were 20–40 s, except Mn, where peak count times were 20–50 s (Supplementary Table 5). Na and K were measured first to minimise loss via devolatilisation. Calibration standards were orthoclase (K, Si and Al), wollastonite (Ca and Si), fayalite (Fe), periclase (Mg), jadeite (Na), tephroite (Mn), rutile (Ti), apatite (P) Cr₂O₃ (Cr), NiO (Ni) and pyrite and anhydrite (S). The basaltic glass standard A99⁶⁵ was used as a secondary standard. Data processing was accomplished using the Probe for EPMA software (v.12.9.5). Analytical precision (1σ as calculated by Probe for EPMA) ranges between <1 and 3% for major elements with concentrations greater than 1%. For major element concentrations <1% analytical precision ranges between 12 and 14%. For element concentrations <0.1%, analytical precision ranges between 41 and 52%. Whole-rock composition of FL samples was determined by measuring four glass chips using EPMA. The reported whole-rock compositions are an average of a number of points (*n* = 30–86) measured from each glass chip. Full compositional data are provided in Supplementary Data 1.

Trace element concentrations were determined using Laser Ablation Inductively Coupled Plasma Mass Spectrometry (LA-ICP-MS) on four samples at the Department of Physics and Geology, Università degli Studi di Perugia, Italy. A Teledyne Photon Machine G2 laser ablation system was used, equipped with a Two-Volume ANU HelEx 2 cell and coupled with a Thermo Fisher Scientific quadrupole-based iCAP Qc ICP-MS spectrometer. We used a circular laser beam, and a beam diameter of either 10–15 µm or 25 µm depending on MI size or microlite density of the glass. The external calibration material was NIST-SRM610. The internal standard was Si. Precision and accuracy were monitored through repeated analyses of the USGS BCR-2-G reference material⁶⁶, analysed as an unknown together with FL and MTL samples over three different analytical sessions. At 25 microns, precision and accuracy are always better than 10% with the only exceptions of Nb and Er, characterized by an accuracy of ~13.6 and ~12%, respectively. At 10–15 microns, precision is always better than 12% with the only exception of Cs (~16%) and Tm (~20%). The accuracy is always better than ~12% with the only exception of Yb (~14%). Complete trace element data are provided in Supplementary Data 3.

Micro-textural analysis. BSE images of MTL samples were also acquired using a FEI Quanta 650 FEG-SEM at the Department of Earth and Environmental Sciences, University of Manchester, applying an acceleration voltage of 15 kV and beam current of 10 nA. We used ImageJ software⁶⁷ for quantitative textural analysis. Crystal fractions were calculated as follows:

$$\phi = \frac{A_x}{A} \quad (1)$$

where A_x represents the area of each crystal phase (*x*) and A , the vesicle-free area of the sample⁶⁸. The crystal fractions presented in this study are all calculated on a vesicle-free basis. The area fraction of enclaves was calculated using the total area, including vesicles.

We used *CSDCorrections* (v.1.6)⁶⁹ to produce CSDs of plagioclase crystals. We used *CSDSlice*⁷⁰ to perform the stereological correction to provide the 3D crystal habit. The CSD graph was used to calculate the crystallisation time (τ) of phenocrysts, microlites and crystals within enclaves, using the linear regression of the slope from the CSD analysis and the following equation⁶⁹.

$$\text{slope} = \frac{-1}{G\tau} \quad (2)$$

where $G\tau$ represents a range of experimentally derived growth rates.

Analysis of volatile concentrations. Volatile concentrations in FL and MTL samples were measured by Secondary Ion Mass Spectrometry (SIMS) at the NERC Ion Microprobe Facility, University of Edinburgh, UK, using a Cameca IMS 7f-Geo instrument. Individual scoria of the FL eruption (2) and MTL eruption (5) hosting phenocrysts were bulk mounted in epoxy resin. MI were only observed in plagioclase. Scoriae were then polished to produce a flat surface suitable for analysis and to expose crystal-hosted MI at the surface. MI were visually inspected prior to analysis using BSE images, and crystallised inclusions were not analysed. Some MI contained fluid bubbles, but most MI analysed are bubble-free. Samples were gold coated prior to analysis and placed under a high vacuum to outgas. Two separate protocols were used to measure CO₂ and H₂O. The first protocol measured ¹²C⁺,

using a primary O⁻ ion beam with an accelerating voltage of 13 keV, a secondary accelerating voltage of 5 keV minus a 50 eV offset, a beam current of 5 nA and a beam diameter of 10 µm. The analysed area was pre-sputtered using the primary beam for 4 min prior to data acquisition. Count times (seconds) are indicated in brackets. The masses ³⁰Si²⁺(2), ⁴⁰Ca²⁺(2) and ²⁴Mg²⁺(5) were also measured alongside ¹²C⁺(10). The interference by ²⁴Mg²⁺ on the ¹²C⁺ peak was resolved by using a high mass resolution configuration of 2997. Masses ³⁰Si⁺ and ⁴⁰Ca²⁺ were acquired to allow comparison with major element data. For the carbon analysis, 15 cycles were acquired, but the first 7 cycles were discarded to minimise the effects from surface contamination. A second protocol was used to measure ¹H⁺, using a primary O⁻ ion beam with an accelerating voltage of 13 keV and secondary accelerating voltage of 5 keV minus 75 eV offset. The analysed area was pre-sputtered for 1 minute prior to data acquisition. The masses ³⁰Si⁺(2), ⁴⁴Ca⁺(5) and ²⁶Mg⁺(2) were also measured alongside ¹H⁺(5), over 10 cycles for each analysis with the beam centred in the pit made by the previous analysis. An extra peak at 0.7(1) was also measured to determine backgrounds for each cycle.

Background counts were monitored by analysing the CO₂ and H₂O-free standard N72, and mean background counts were subtracted from acquired data. Calibration curves for H₂O and CO₂ (Supplementary Fig. 7) were constructed using the measured background-corrected counts per second of a suite of tholeiitic basaltic glass standards (M40, N72, M36, M21, M5, M10 and M47)⁷¹, considering the SiO₂ content. H₂O and CO₂ contents of unknowns were then calculated using their background-corrected counts per second and the measured SiO₂ concentration of the MI, as determined by EPMA. The EPMA analysis was performed after the SIMS analysis, to avoid surface contamination from carbon coating the samples. Precision (1σ) was calculated through repeat measurements of the standard array and is ±3% for CO₂ and ±2% for H₂O. Accuracy (1σ) is ±13% for CO₂ and ±5% for H₂O across the standard array, calculated by comparing measured compositions with published values. Images of MI and phenocryst hosts can be found in the Supplementary Information (Supplementary Figs. 10–21). Phenocryst, MI and bubble sizes can be found in Supplementary Data 1.

Post-entrapment crystallisation correction of melt inclusions. Plagioclase-hosted MI were corrected for post-entrapment crystallisation (PEC) following Neave et al.⁷². The plagioclase-melt equilibrium model of Putirka⁴⁶, which accounts for the effect of H₂O on equilibration, was used to calculate the plagioclase composition in equilibrium with the melt. This equilibrium plagioclase composition was then added incrementally to the measured MI composition. For FL MI, the PEC correction is achieved when the corrected composition matches the SiO₂-FeO systematics predicted by a linear regression through glass data from this study and Costantini et al.¹⁰ on the FL eruption. For MTL MI, we matched the PEC-corrected compositions to the MgO-Al₂O₃ systematics predicted by a linear regression through glass data of the MTL eruption¹⁶. The mean PEC correction for FL MI is 3% (range 0–8%). The mean PEC correction for MTL MI is 3% (range 0–14%). This correction was then extended to volatile elements, which are assumed to be incompatible. The correction was also extended to trace element compositions, which were corrected based on their compatibility in plagioclase, evaluated using experimental partition coefficients on plagioclase-melt partitioning for basaltic melts^{73–75}. All trace elements were corrected as incompatible except Sr, Cs and Pb. Raw and corrected MI compositions are presented in Supplementary Data 1 and 3.

Geochemical modelling. Rhyolite-MELTS simulations were performed using the average PEC-corrected FL MI composition, with f_{O_2} fixed at NNO-0.65, consistent with the results of Bamber et al.¹⁶, to determine the pressure-temperature window for the pre-eruptive storage condition. We performed simulations between fixed pressures of 100–10 MPa, with a pressure step of 10 MPa (Supplementary Fig. 8). The Moore et al.⁷⁶ model was used as an initial test to calculate the input H₂O content (Supplementary Fig. 9). Isobaric simulations were performed under volatile-saturated conditions, using the MagmaSat solubility model incorporated in Rhyolite-MELTS⁴¹. The temperature investigated ranged between 1150 and 950 °C, with a temperature step of 1 °C. For the liquid line of descent (LLD) model, isobaric simulations were performed at 40 MPa and 200 MPa with initial H₂O fixed at 2.3 wt.% and 5.2 wt.% respectively, to maintain H₂O-saturated conditions. The initial CO₂ was 0.12 wt.%. Simulations were performed between temperatures of 1080–960 °C with a step of 5 °C.

Isobars were produced using the MagmaSat software⁴¹. The average PEC-corrected MI composition was used to produce H₂O-CO₂ isobars for the FL samples. Temperature was fixed at 1060 °C, consistent with mineral-melt thermometry results from this study and the maximum experimentally determined pre-eruptive temperature¹¹. The average MTL MI composition¹⁶ was used to construct the MTL H₂O-CO₂ isobars, instead with temperature fixed at 1100 °C, consistent with the maximum temperature defined for the MTL pre-eruptive condition from petrological analysis¹⁶. Saturation pressure calculations were performed using MagmaSat, with an input temperature of 1060 °C for FL MI and an input temperature of 1100 °C for MTL MI. All MagmaSat calculations were performed using the software VESCAL⁴².

The fractional crystallisation model was produced using Petrograph software³⁴ and uses a D_{Zr} partition coefficient of 0.001. D_{Sr} is 1.714, D_{Ba} is 0.327 and D_{La} is 0.061⁷³. The partition coefficients used were obtained from the experiments of

Aigner-Torres et al.⁷³ on trace element partitioning between plagioclase and basaltic melt. These experiments were selected as the whole-rock composition used and the experimental conditions investigated (1180 °C, NNO-0.75) can be considered representative of the FL pre-eruptive conditions. As plagioclase is the dominant crystallising phase, we assume that plagioclase partition coefficients are representative of the bulk partition coefficient for the assemblage. As a linear trend can only be defined for the FL, a fractional crystallisation trend was modelled only for this eruption, using the most primitive MI as the starting composition.

Mineral-melt thermometry. We used equation 23 of Putirka⁴⁶ and an input water content of 2.27 wt.% to determine the temperature of plagioclase crystallisation for the FL eruption. We also performed calculations using a lower water content of 1.59 wt.%, calculated as an average H₂O content from MI of this study, Goepfert and Gardner¹¹ and Wehrmann et al.⁴⁵. The standard error of the thermometer is ±43 °C. The K_D (Ab-An) equilibrium criterion (0.28 ± 0.11 for $T > 1050$ °C and 0.1 ± 0.05 for $T < 1050$ °C) was used to test for plagioclase-melt equilibrium. We used an input pressure of 80 MPa, the maximum experimentally determined pre-eruptive storage pressure¹¹. We used equation 33 of Putirka⁴⁶ and the same input pressure conditions to determine the temperature of pyroxene crystallisation. The standard error of the thermometer is ±45 °C. The K_D (Fe-Mg) equilibrium criterion (0.28 ± 0.08) was used to test for clinopyroxene-melt equilibrium.

Constitutive equations of the 1D steady-state conduit model. To simulate basaltic Plinian eruptions at Las Sierras-Masaya Volcanic system, we use the 1D steady-state model of La Spina et al.^{25–27}, which simulates magma ascent within a cylindrical conduit. The governing equations of the model are provided in the Supplementary Methods. The model is presented in a general form which can be applied to a variety of volcanoes and eruptive styles^{25–27}. To simulate the basaltic Plinian eruptions of Las Sierras-Masaya volcanic system, a series of constitutive equations must be defined to describe the magma ascent dynamics for this particular volcanic system and regime, including rheological, crystallisation, volatile solubility, outgassing, wall-friction, and fragmentation models.

The rheology of the magmatic mixture has been modelled following La Spina et al.⁶⁴. The mixture viscosity is calculated as a function of the crystal-free, bubble-free melt viscosity, multiplied by two factors which account for crystals and bubbles. The viscosity of the melt phase is calculated following Giordano et al.⁷⁷. We used the average MTL MI composition (Supplementary Table 6) as the melt composition¹⁶.

We account for the effect of bubbles on the mixture viscosity following Llewellyn et al.⁷⁸, Mader et al.⁷⁹ and La Spina et al.⁶⁴. The effect on mixture viscosity is controlled by the capillary number (Ca), a dimensionless number that describes the ratio between the relaxation time of the bubble in response to deformation and the timescale of deformation in the fluid⁷⁹. At low capillary numbers, bubbles tend to be spherical, whereas at high capillary numbers they are highly elongated. As the MTL samples dominantly show spherical bubbles, for our simulations we assume $Ca \ll 1$.

The crystallisation model considers plagioclase, clinopyroxene and olivine. It is assumed that no crystals are removed during ascent. Similarly, to La Spina et al.²⁵, the equilibrium mass fraction x_j^{eq} of each crystal phase j is calculated using the polynomial function:

$$x_j^{eq}(T^*, x_d^*) = \zeta_{j,1} \cdot (T^*)^2 + \zeta_{j,2} \cdot (x_d^*)^2 + \zeta_{j,3} \cdot T^* \cdot x_d^* + \zeta_{j,4} \cdot T^* + \zeta_{j,5} \cdot x_d^* + \zeta_{j,6} \quad (3)$$

where T^* is the temperature of the liquid in °C and x_d^* is the water content dissolved in the liquid in weight percent. With respect to La Spina et al.²⁵, we neglect all terms related to pressure in the polynomial function, since we only consider water-saturated conditions. The coefficients $\zeta_{i,j}$ are provided in Supplementary Table 7. We also account for disequilibrium crystallisation, as it is likely that there is rapid syn-eruptive crystallisation^{15,16}. The characteristic time of crystallisation $\tau^{(c)}$ is set to 10 s¹⁵.

The solubility model for water and carbon dioxide has been described following Henry's Law for gas mixtures¹⁵. The solubility parameters controlling the equilibrium dissolved mass fraction of gas follow Arzilli et al.¹⁵.

Outgassing has been described following La Spina et al.²⁶. The degree of decoupling between gas and melt is controlled by the relaxation parameter $\tau^{(f)}$, which is defined to consider a permeability model based on Forchheimer's law below the fragmentation level, and Stokes' law elsewhere²⁶. The parameters controlling $\tau^{(f)}$ follow La Spina et al.²⁷.

To simulate fragmentation during magma ascent, we adopt the strain-rate criterion of Papale³³. Failure of the magma occurs when the Deborah number (the ratio between the Maxwell relaxation timescale and the timescale of deformation) exceeds 0.01²⁷.

The pre-eruptive storage chamber for the Plinian eruptions of Masaya caldera is estimated at a depth of ~2 km^{13,16}. Geophysical investigation of the present Masaya plumbing system resolves a magma body with a depth-to-centre of ~3 km²⁴. Due to the similarity of the estimated reservoir depth for both Plinian and present-day activity, we use an initial pressure estimate of 42 MPa for our simulations¹⁶. Results can be found in Supplementary Data 4.

Sensitivity analysis. The sensitivity analysis was performed using the open-source software DAKOTA toolkit (Design Analysis Kit for Optimization and Terascale Applications)⁸⁰ developed at Sandia National Laboratories. We selected a range of values for the input parameters which incorporate the pre-eruptive conditions determined for the eruptions of Las Sierras-Masaya volcanic system: FL, SAT, MTL and MT-TII^{3,10,11,13,16,21} and recent activity at Masaya caldera^{20,23} (Supplementary Table 8). The sensitivity analysis was performed using 10,000 simulations with different combinations of the input parameters, varied assuming a uniform distribution within the aforementioned ranges. Results of the sensitivity analysis can be found in Supplementary Data 5.

Chamber volume calculation. We estimate the magma chamber volume following the method of La Spina et al.⁶⁴, coupling the steady-state conduit flow model with a quasi steady-state model of the chamber. The following equation describes the variation in pressure through time as a function of the chamber volume and mass eruption rate^{81–83}.

$$\frac{\partial p_{ch}}{\partial t} = \frac{4EK}{\rho V_{ch}(3K + 4E)} (Q_{in} - Q_{out}) \quad (4)$$

The pressure of the magma chamber is indicated by p_{ch} , the volume by V_{ch} , E is the elastic modulus of the country rock, K is the bulk modulus of the magma and ρ is the average magma density. We use an elastic modulus of $E = 2 \times 10^{10}$ Pa, a bulk modulus of $K = 10^{10}$ Pa and an average magma density of $\rho = 2700 \text{ kg m}^{-3}$ ⁵¹. The mass flow rate is represented by Q , however, we assume negligible input into the magma chamber (Q_{in}), thereby setting Q_{in} to 0. The magma flux out of the chamber is represented by Q_{out} .

We use the 1D steady-state conduit model to perform multiple simulations with the inlet pressure decreasing accordingly with Eq. (4) and use the computed mass flow rates at each pressure step in our calculation. We stop the simulations when the pressure within the conduit is too low to maintain conduit stability and collapse of the conduit walls is expected to occur, which we assume represents the end of the eruption. The collapse of the conduit wall is predicted following the Mohr-Coulomb criteria^{64,84}. Simulations were performed using both endmembers of the MTL eruption. As a first order approximation, we determine the eruption duration for three estimates of chamber volume: 1 km³, 10 km³ and 100 km³. We assume that the most probable order of magnitude estimate of the magma chamber volume is that which shows the best agreement with the estimated eruption duration and erupted volume, taken as a range which accounts for both endmembers.

Data availability

All analytical data supporting the findings of this study are provided within the article and Supplementary Data. This data and the data produced by numerical simulations are available at <https://doi.org/10.6084/m9.figshare.20764858>.

Code availability

The magma ascent model used in this study has been adapted from the MAMMA model available on GitHub: <https://github.com/demichie/MAMMA>. The version of the MAMMA model used in this work is available at <https://doi.org/10.6084/m9.figshare.20764858>.

Received: 11 October 2021; Accepted: 12 October 2022;
Published online: 29 October 2022

References

- Williams, S. N. Plinian airfall deposits of basaltic composition. *Geology* **11**, 211–214 (1983).
- Costantini, L., Bonadonna, C., Houghton, B. & Wehrmann, H. New physical characterization of the Fontana Lapilli basaltic Plinian eruption, Nicaragua. *Bull. Volcanol.* **71**, 337–355 (2009).
- Pérez, W., Freundt, A., Kutterolf, S. & Schmincke, H. The Masaya Triple Layer: A 2100 year old basaltic multi-episodic Plinian eruption from the Masaya Caldera Complex (Nicaragua). *J. Volcanol. Geotherm. Res.* **179**, 191–205 (2009).
- Coltelli, M., Del Carlo, P. & Vezzoli, L. Discovery of a Plinian basaltic eruption of Roman age at Etna volcano, Italy. *Geology* **26**, 1095–1098 (1998).
- Walker, G. P. L., Self, S. & Wilson, L. Tarawera 1886, New Zealand – a basaltic Plinian fissure eruption. *J. Volcanol. Geotherm. Res.* **21**, 61–78 (1984).
- Alfano, F. et al. Subplinian monogenetic basaltic eruption of Sunset Crater, Arizona, USA. *Geol. Soc. Am. Bull.* **131**, 661–674 (2018).
- Moussallam, Y. et al. Fast ascent rate during the 2017–2018 Plinian eruption of Ambae (Aoba) volcano: a petrological investigation. *Contrib. Mineral. Petrol.* **174**, 1–24 (2019).

8. Sable, J. E., Houghton, B. F., Del Carlo, P. & Coltelli, M. Changing conditions of magma ascent and fragmentation during the Etna 122 BC basaltic Plinian eruption: Evidence from clast microtextures. *J. Volcanol. Geotherm. Res.* **158**, 333–354 (2006).
9. Sable, J., Houghton, B., Wilson, C. & Carey, R. *Eruption mechanisms during the climax of the Tarawera 1886 basaltic Plinian eruption inferred from microtextural characteristics of the deposits.* (Stud. Volcanology: Leg. George Walk. Spec. Publ. IAVCEI 2, Geological Society, 2009).
10. Costantini, L., Houghton, B. & Bonadonna, C. Constraints on eruption dynamics of basaltic explosive activity derived from chemical and microtextural study: The example of the Fontana Lapilli Plinian eruption, Nicaragua. *J. Volcanol. Geotherm. Res.* **189**, 207–224 (2010).
11. Goepfert, K. & Gardner, J. Influence of pre-eruptive storage conditions and volatile contents on explosive Plinian style eruptions of basic magma. *Bull. Volcanol.* **72**, 511–521 (2010).
12. Szramek, L. Mafic Plinian eruptions: is fast ascent required? *J. Geophys. Res. Solid Earth* **121**, 7119–7136 (2016).
13. Pérez, W., Freundt, A. & Kutterolf, S. The basaltic Plinian eruption of the ~6 ka San Antonio Tephra and formation of the Masaya caldera, Nicaragua. *J. Volcanol. Geotherm. Res.* **401**, 106975 (2020).
14. Moitra, P., Gonnerman, H. M., Houghton, B. F. & Tiwary, C. S. Fragmentation and Plinian eruption of crystallizing basaltic magma. *Earth Planet. Sci. Lett.* **500**, 97–104 (2018).
15. Arzilli, F. et al. Magma fragmentation in highly explosive basaltic eruptions induced by rapid crystallization. *Nat. Geosci.* **12**, 1023–1028 (2019a).
16. Bamber, E. C. et al. Pre- and syn-eruptive conditions of a basaltic Plinian eruption at Masaya Volcano, Nicaragua. *J. Volcanol. Geotherm. Res.* **392**, 106761 (2020).
17. Di Genova, D. et al. In situ observation of nanolite growth in volcanic melt: A driving force for explosive eruptions. *Sci. Adv.* **6**, eabb0413 (2020).
18. Girard, G. & van Wyk de Vries, B. The Managua Graben and Las Sierras-Masaya volcanic complex (Nicaragua); pull-apart localization by an intrusive complex: results from analogue modelling. *J. Volcanol. Geotherm. Res.* **144**, 37–57 (2005).
19. Burton, M. R., Oppenheimer, C., Horrocks, L. A. & Francis, P. W. Remote sensing of CO₂ and H₂O emission rates from Masaya volcano, Nicaragua. *Geology* **28**, 915–918 (2000).
20. Zurek, J., Moune, S., Williams-Jones, G., Vigouroux, N. & Gauthier, P.-J. Melt inclusion evidence for long term steady-state volcanism at Las Sierras-Masaya volcano, Nicaragua. *J. Volcanol. Geotherm. Res.* **378**, 16–28 (2019).
21. Pérez, W. Basaltic Plinian and violent Surtseyan eruptions from the Masaya Caldera Complex, Nicaragua. *PhD thesis*, University of Kiel, 195 (2007).
22. Walker, J. A., Williams, S. N., Kalamarides, R. I. & Feigenson, M. D. Shallow open-system evolution of basaltic magma beneath a subduction zone volcano: the Masaya Caldera Complex, Nicaragua. *J. Volcanol. Geotherm. Res.* **56**, 379–400 (1993).
23. Hlinka, L., Longpré, M.-A., Pérez, W., Kutterolf, S. & Monteleone, B. Top-down control on eruptive style at Masaya volcano inferred from melt composition. *Earth Planet. Sci. Lett.* **572**, 117138 (2021).
24. Stephens, K. J. & Wauthier, C. Satellite geodesy captures offset magma supply associated with lava lake appearance at Masaya volcano, Nicaragua. *Geophys. Res. Lett.* **45**, 2669–2678 (2018).
25. La Spina, G., Burton, M. & de' Michieli Vitturi, M. Temperature evolution during magma ascent in basaltic effusive eruptions: a numerical application to Stromboli volcano. *Earth Planet. Sci. Lett.* **426**, 89–100 (2015).
26. La Spina, G., Polacci, M., Burton, M. & de' Michieli Vitturi, M. Numerical investigation of permeability models for low viscosity magmas: Application to the 2007 Stromboli effusive eruption. *Earth Planet. Sci. Lett.* **473**, 279–290 (2017).
27. La Spina, G. et al. Explosivity of basaltic lava fountains is controlled by magma rheology, ascent rate and outgassing. *Earth Planet. Sci. Lett.* **553**, 116658 (2021).
28. Freundt, A. & Schmincke, H.-U. Mixing of rhyolite, trachyte and basalt magma erupted from a vertically and laterally zoned reservoir, composite flow P1, Gran Canaria. *Contrib. Mineral. Petrol.* **112**, 1–19 (1992).
29. Hermes, O. D. & Cornell, W. C. Quenched crystal mush and associated magma compositions as indicated by intercumulus glasses from Mt. Vesuvius, Italy. *J. Volcanol. Geotherm. Res.* **9**, 133–149 (1981).
30. Ellis, B. S., Bachmann, O. & Wolff, J. A. Cumulate fragments in silicic ignimbrites: the case of the Snake River Plain. *Geology* **42**, 431–434 (2014).
31. Pistone, M. et al. Gas-driven filter pressing in magmas: Insights into in-situ melt segregation from crystal mushes. *Geology* **43**, 699–702 (2015).
32. Marsh, B. D. *Magma chambers.* (Encycl. of Volcan. San Diego, California, Academic Press, 2015).
33. Gualda, G. A. R., Ghiorso, M. S., Lemons, R. V. & Carley, T. Rhyolite-MELTS: a modified calibration of MELTS optimized for silica-rich, fluid-bearing magmatic systems. *J. Petrol.* **53**, 875–890 (2012).
34. Petrelli, M., Poli, G., Perugini, D. & Peccerillo, A. PetroGraph: a new software to visualize, model, and present geochemical data in igneous petrology. *Geochem. Geophys. Geosyst.* **6**, Q07011 (2005).
35. Lissenberg, C. J., MacLeod, C. J. & Bennett, E. N. Consequences of a crystal mush-dominated magma plumbing system: a mid-ocean ridge perspective. *Philos. Trans. R. Soc. A*, **377**, 20180014 (2018).
36. Arzilli, F. et al. The unexpected explosive sub-Plinian eruption of Calbuco volcano (22–23 April 2015; southern Chile): triggering mechanism implications. *J. Volcanol. Geotherm. Res.* **378**, 35–50 (2019b).
37. Moore, L. R. et al. Bubbles matter: an assessment of the contribution of vapor bubbles to melt inclusion volatile budgets. *Am. Mineral.* **100**, 806–823 (2015).
38. Wieser, P. E. et al. Reconstructing magma storage depths for the 2018 Kilauean eruption from melt inclusion CO₂ contents: the importance of vapor bubbles. *Geochem. Geophys. Geosyst.* **22**, e2020GC009364 (2021).
39. Rasmussen, D. J., Plank, T. A., Wallace, P. J., Newcombe, M. E. & Lowenstern, J. B. Vapor-bubble growth in olivine-hosted melt inclusions. *Am. Mineral.* **105**, 1898–1919 (2020).
40. Hartley, M. E., MacLennan, J., Edmonds, M. & Thordarson, T. Reconstructing the deep CO₂ degassing behaviour of large basaltic fissure eruptions. *Earth Planet. Sci. Lett.* **393**, 120–131 (2014).
41. Ghiorso, M. S. & Gualda, G. A. R. An H₂O-CO₂ mixed fluid saturation model compatible with rhyolite-MELTS. *Contrib. Mineral. Petrol.* **169**, 1–30 (2015).
42. Iacovino, K., Matthews, S., Wieser, P. E., Moore, G. M. & Bégue, F. VESICAL Part I: an open-source thermodynamic model engine for mixed volatile (H₂O-CO₂) solubility in silicate melts. *Earth Space Sci.* **8**, e2020EA001584 (2021).
43. Lloyd, A. S., Plank, T., Ruprecht, P., Hauri, E. H. & Rose, W. Volatile loss from melt inclusions in pyroclasts of differing sizes. *Contrib. Mineral. Petrol.* **165**, 129–153 (2013).
44. Qin, Z., Lu, F. & Anderson, A. T. Diffusive re-equilibration of melt and fluid inclusions. *Am. Mineral.* **77**, 565–576 (1992).
45. Wehrmann, H., Hoernle, K., Portnyagin, M., Wiedenbeck, M. & Heydolph, K. Volcanic CO₂ output at the Central American subduction zone inferred from melt inclusions in olivine crystals from mafic tephros. *Geochem. Geophys. Geosyst.* **12**, Q06003 (2011).
46. Putirka, K. D. Thermometers and barometers for volcanic systems. *Rev. Mineral. Geochem.* **69**, 61–120 (2008).
47. Zellmer, G. F. Gaining acuity on crystal terminology in volcanic rocks. *Bull. Volcanol.* **83**, 78 (2021).
48. Gutiérrez, F. & Parada, M. A. Numerical modeling of time-dependent fluid dynamics and differentiation of a shallow basaltic magma chamber. *J. Petrol.* **51**, 731–762 (2010).
49. Cooper, K. M. Time scales and temperatures of crystal storage in magma reservoirs: implications for magma reservoir dynamics. *Philos. Trans. R. Soc. A*, **377**, 20180009 (2019).
50. Albert, H. et al. Magma interactions, crystal mush formation, timescales and unrest during caldera collapse and lateral eruption at ocean island basaltic volcanoes (Piton de la Fournaise, La Réunion). *Earth Planet. Sci. Lett.* **515**, 187–199 (2019).
51. Tait, S., Jaupart, C. & Vergnolle, S. Pressure, gas content and eruption periodicity of a shallow, crystallising magma chamber. *Earth Planet. Sci. Lett.* **92**, 107–123 (1989).
52. Tramontano, S., Gualda, G. A. R. & Ghiorso, M. S. Internal triggering of volcanic eruptions: tracking overpressure regimes for giant magma bodies. *Earth Planet. Sci. Lett.* **472**, 142–151 (2017).
53. Papale, P. Strain-induced magma fragmentation in explosive eruptions. *Nature* **397**, 425–428 (1999).
54. Shea, T. Bubble nucleation in magmas: a dominantly heterogeneous process? *J. Volcanol. Geotherm. Res.* **343**, 155–170 (2017).
55. Cimarelli, C., Di Traglia, F. & Taddeucci, J. Basaltic scoria textures from a zoned conduit as precursors to violent Strombolian activity. *Geology* **38**, 439–442 (2011).
56. Taddeucci, J., Pompilio, M. & Scarlato, P. Conduit processes during the July–August 2001 explosive activity of Mt. Etna (Italy): inferences from glass chemistry and crystal size distribution of ash particles. *J. Volcanol. Geotherm. Res.* **137**, 33–54 (2004).
57. Caravantes González, G. et al. Structures controlling volcanic activity within Masaya caldera, Nicaragua. *Volcanica* **2**, 25–44 (2019).
58. Allison, C., Roggensack, K. & Clarke, A. B. Highly explosive basaltic eruptions driven by CO₂ exsolution. *Nat. Commun.* **12**, 217 (2021).
59. Allard, P. A CO₂-rich gas trigger of explosive paroxysms at Stromboli basaltic volcano, Italy. *J. Volcanol. Geotherm. Res.* **189**, 363–374 (2010).
60. Freundt, A. & Tait, S. R. The entrainment of high-viscosity magma into low-viscosity magma in eruption conduits. *Bull. Volcanol.* **48**, 325–339 (1986).
61. Blake, S. & Campbell, I. H. The dynamics of magma-mixing during flow in volcanic conduits. *Contrib. Mineral. Petrol.* **94**, 72–81 (1986).
62. Ubide, T. & Kamber, B. S. Volcanic crystals as time capsules of eruption history. *Nat. Commun.* **9**, 326 (2018).

63. Moretti, R. et al. Degassing vs eruptive styles at Mt. Etna volcano (Sicily, Italy). Part I: Volatile stocking, gas fluxing, and the shift from low-energy to highly explosive basaltic eruptions. *Chem. Geol.* **482**, 1–17 (2018).
64. La Spina, G. et al. Conduit dynamics of highly explosive basaltic eruptions: the 1085 CE Sunset Crater sub-Plinian events. *J. Volcanol. Geotherm. Res.* **387**, 106658 (2019).
65. Jarosewich, E., Nelen, J. A. & Norberg, J. A. Reference samples for electron microprobe analysis. *Geostandards Newsletter* **4**, 43–47 (1980).
66. Rocholl, A. Major and trace element composition and homogeneity of microbeam reference material: Basalt glass USGS BCR-2G. *Geostan. Geanaly. Res.* **22**, 33–45 (1998).
67. Abramoff, M. D., Magalhães, P. J. & Ram, S. J. Image processing with ImageJ. *Biophoton. Int.* **11**, 36–42 (2004).
68. Hammer, J. E., Cashman, K. V., Hoblitt, R. P. & Newman, S. Degassing and microcline crystallization during pre-climatic events of the 1991 eruption of Mt. Pinatubo, Philippines. *Bull. Volcanol.* **60**, 875–890 (1999).
69. Higgins, M. D. Measurements of crystal size distributions. *Am. Mineral.* **85**, 1105–1116 (2000).
70. Morgan, D. & Jerram, D. On estimating crystal shape for crystal size distribution analysis. *J. Volcanol. Geotherm. Res.* **154**, 1–7 (2006).
71. Shishkina, T. A., Botcharnikov, R. E., Holtz, F., Almeev, R. R. & Portnyagin, M. V. Solubility of H₂O- and CO₂-bearing fluids in theolitic basalts at pressures up to 500 MPa. *Chem. Geol.* **277**, 115–125 (2010).
72. Neave, D. A., Hartley, M. E., MacLennan, J., Edmonds, M. & Thordarson, T. Volatile and light lithophile elements in high-anorthite plagioclase-hosted melt inclusions from Iceland. *Geochim. Cosmochim. Acta.* **205**, 100–118 (2017).
73. Aigner-Torres, M., Blundy, J., Ulmer, P. & Pettke, T. Laser Ablation ICPMS study of trace element partitioning between plagioclase and basaltic melts: an experimental approach. *Contrib. Mineral. Petrol.* **153**, 647–667 (2007).
74. Bindemann, I. N., Davis, A. M. & Drake, M. J. Ion microprobe study of plagioclase-basalt partition experiments at natural concentration levels of trace elements. *Geochim. Cosmochim. Acta.* **62**, 1175–1193 (1998).
75. Laubier, M., Grove, T. L. & Langmuir, C. H. Trace element mineral/melt partitioning for basaltic and basaltic andesitic melts: an experimental and laser ICP-MS study with application to the oxidation state of mantle source regions. *Earth Planet. Sci. Lett.* **392**, 265–278 (2014).
76. Moore, G., Vennemann, T. & Carmichael, I. S. E. An empirical model for solubility of H₂O in magmas to 3 kilobars. *Am. Mineral.* **83**, 36–42 (1998).
77. Giordano, D., Russell, J. K. & Dingwell, D. B. Viscosity of magmatic liquids: a model. *Earth Planet. Sci. Lett.* **271**, 123–134 (2008).
78. Llewellyn, E. W., Mader, H. M. & Wilson, S. D. R. The constitutive equation and flow dynamics of bubbly magmas. *Geophys. Res. Lett.* **29**, 2170 (2002).
79. Mader, H. M., Llewellyn, E. W. & Mueller, S. P. The rheology of two-phase magmas: a review and analysis. *J. Volcanol. Geotherm. Res.* **257**, 135–158 (2013).
80. Adams, B. M. et al. Multilevel parallel object-oriented framework for design optimization, parameter estimation, uncertainty quantification, and sensitivity analysis version 6.6. *User's Manual*. Technical report, SAND2014-4633 (Sandia National Laboratories, 2017).
81. Woods, A. W. & Koyaguchi, T. Transitions between explosive and effusive eruptions of silicic magmas. *Nature* **370**, 641–644 (1994).
82. Melnik, O. Dynamics of two-phase conduit flow of high-viscosity gas-saturated magma: large variations of sustained explosive eruption intensity. *Bull. Volcanol.* **62**, 153–170 (2000).
83. Melnik, O. & Sparks, R. S. J. Controls on conduit magma flow dynamics during lava dome building eruptions. *J. Geophys. Res.* **110**, B02209 (2005).
84. Aravena, Á., de' Michieli Vitturi, M., Cioni, R. & Neri, A. Stability of volcanic conduits during explosive eruptions. *J. Volcanol. Geotherm. Res.* **339**, 52–62 (2017).
85. Ryan, W. B. F. et al. Global Multi-Resolution Topography synthesis. *Geochem. Geophys. Geosyst.* **10**, Q03014 (2009).

Acknowledgements

The work contained in this publication contains work conducted during a PhD study supported by the Natural Environment Research Council (NERC) EAO Doctoral Training Partnership and is fully funded by NERC whose support is gratefully acknowledged (Grant Number NE/L002469/1). We acknowledge the RCUK NERC-NSFGeo DisEqm project (NE/N018575/1), and support from INGV Pisa from a CASE studentship. F.A. thanks the KINETICVOLC project funded by the European Union, NextGenerationEU, Ministry of University and Research, Promotion and Development Fund DM737/2021. We thank Instituto Nicaragüense de Estudios Territoriales (INETER), J.A. Saballos and D. Chavarría for their extensive and valuable assistance during fieldwork in Nicaragua. Access to the Edinburgh Ion Microprobe Facility was supported by NERC grant IMF686/0519 to MRB, and we thank C. Talavera and J. Craven for their assistance with the SIMS analyses. We thank the University of Perugia for use of their LA-ICP-MS facility, and D. Perugini and D. Morgavi for insightful discussions, laboratory access and assistance with sample preparation. We thank D.A. Neave for assistance with post-entrainment crystallisation corrections. Sensitivity analyses were performed using the ARCHER2 National Supercomputing Service.

Author contributions

E.C.B. conceived the research project with G.L.S., F.A., M.Po., M.B., M.E.H. and M.M.V. E.C.B., M.Po and F.A. collected the Masaya samples. E.C.B. performed the numerical simulations with G.L.S. and M.M.V. E.C.B. performed the chemical analyses with F.A., M.E.H., and J.F. M.Pe performed the LA-ICP-MS analysis with E.C.B. All authors contributed to production of the manuscript.

Competing interests

The authors declare no competing interests.

Additional information

Supplementary information The online version contains supplementary material available at <https://doi.org/10.1038/s43247-022-00585-5>.

Correspondence and requests for materials should be addressed to Emily C. Bamber.

Peer review information *Communications Earth & Environment* thanks Penny Wieser, Ery Hughes and the other, anonymous, reviewer(s) for their contribution to the peer review of this work. Primary Handling Editors: Emma Liu, Joe Aslin.

Reprints and permission information is available at <http://www.nature.com/reprints>

Publisher's note Springer Nature remains neutral with regard to jurisdictional claims in published maps and institutional affiliations.



Open Access This article is licensed under a Creative Commons Attribution 4.0 International License, which permits use, sharing, adaptation, distribution and reproduction in any medium or format, as long as you give appropriate credit to the original author(s) and the source, provide a link to the Creative Commons license, and indicate if changes were made. The images or other third party material in this article are included in the article's Creative Commons license, unless indicated otherwise in a credit line to the material. If material is not included in the article's Creative Commons license and your intended use is not permitted by statutory regulation or exceeds the permitted use, you will need to obtain permission directly from the copyright holder. To view a copy of this license, visit <http://creativecommons.org/licenses/by/4.0/>.

© The Author(s) 2022